

# INFN Genova Study for the PANDA Solenoid Magnet

Andrea Bersani, Andrea Pastorino, Renzo Parodi  
*INFN Genova Division*  
Via Dodecaneso 33, 16146, Genova

## **Contents:**

- Solenoid Magnet and Flux Return for the PANDA Detector
- Mechanical and Thermal Design for the PANDA Superconducting Solenoid Coil
- Annex A: Material Properties
- Annex B: Preliminary Technical Drawings

# Solenoid Magnet and Flux Return for the PANDA Detector

Andrea Bersani, Renzo Parodi, Andrea Pastorino

Istituto Nazionale di Fisica Nucleare, Sezione di Genova

Via Dodecaneso 33, 16146-Genova (Italy)

March 6, 2007

## Abstract

In this paper we present the project of the Solenoid Magnet for the PANDA detector developed in Genova. This project foresees a coil realized with a Rutherford-type, aluminum stabilized superconducting cable, wound inside an aluminum coil former and indirectly cooled with a forced circulation of liquid helium. The concept of this magnet is the same of many other working magnet used in different detectors, such as, for example, BaBar, Finuda, Delphi or CMS. A complete characterization of the magnetic, mechanical and thermal properties of the magnet is presented, with an ansatz on the time schedule to be followed to fulfill the detector deadlines.

## 1 Physics Requirements and Performance Goals

The PANDA target magnet<sup>1</sup> is a thin, superconducting solenoid with an octagonal flux return yoke, as shown in fig. 1. Detector performance criteria and geometry considerations drive the design of the solenoid and the flux return. The magnitude and uniformity specifications for the magnetic field are derived from the tracker requirements: to achieve a mass resolution of the

---

<sup>1</sup>This work has been partly supported by the EU FP6 under the “DIRAC secondary beam” project, contract N. 515873.

order of 10 MeV a magnetic field of 2 T is needed. The combined thickness of the vertex detector, outer tracker, particle identification system, electromagnetic calorimeter and appropriate clearances sets the cryostat inner diameter. Cryostat length is also constrained by the length of the nested subsystems. The solenoid thickness has to be taken into account when evaluating the detection threshold of muons in the chambers hosted inside and outside the flux return yoke.

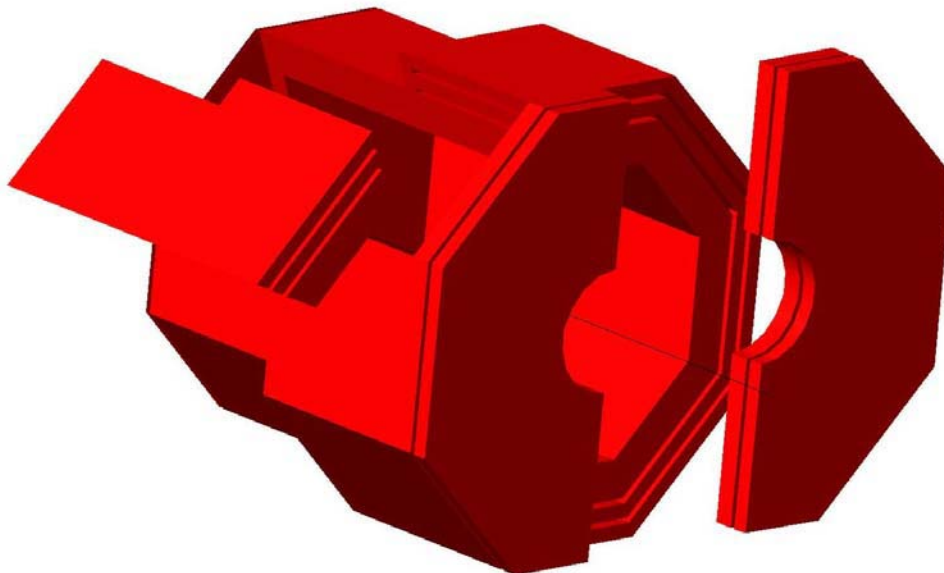


**Figure 1:** The yoke layout: in this picture, the front door is open and one sector is out from its work position.

The shape of the downstream region of the yoke has been designed to allow the installation of several layers of muon chambers: a rough tracking of outgoing muons will be achieved thanks to this superlayer of steel and sensitive elements.

The minimum thickness in the barrel and in the end caps is calculated to avoid magnetic saturation and to stop pions: this is evaluated  $\sim 40$  cm. End caps segmentation was studied to clamp the fringe fields without an excessive increase of the amount of steel involved. Separation and movement of the end doors are constrained by beam line components, by the presence

of the dipole magnet in downstream direction and by the need to provide ready access to detector subsystems.

The physics performance and operational requirements for the solenoid magnet and for the flux return (tables 1 and 2) are similar to those of many operating detector magnets.

<b>Solenoid Requirements</b>	
Central induction	2 T
Uniformity in outer tracker	$\pm 2\%$
Nuclear interaction length	$0.4\lambda_{int}$
Cryostat inner radius	950 mm
Cryostat outer radius	1340 mm
Minimization of thermal cycling	

<b>Flux return Requirements</b>	
Provide an external path for the magnetic field	
Provide support and stopping for muon chambers	
Provide gravitational load for the detector	
Movable end doors to allow access inside the barrel	

**Table 1:** Physics performances and operational requirements for the PANDA solenoid.

## 2 Overview

The design of the superconducting coil for the PANDA experiment is conservative and within the state of the art for detector magnets. It is based on the experience gained over the past 25 years with thin superconducting solenoids. Although specifically tailored to meet the requirements of PANDA, this design is similar to many operating detector magnets. A common feature of all these magnets is the use of aluminum-stabilized conductors that are indirectly cooled by liquid helium pipes connected to an aluminum alloy support structure. This technique was first developed for CELLO[1], the first thin solenoid, and has been improved in subsequent designs. Table 2 shows the main features of some of these solenoid compared to the PANDA design. All these designs used a Rutherford-type cable made of NbTi superconductor encased in an aluminum stabilizer that allows for adequate quench protection.

	ZEUS	ALEPH	BABAR	PANDA
Location	DESY	CERN	SLAC	GSI
Manufacturer	Ansaldo	Saclay	Ansaldo	?
Year completed	1988	1986	1997	2010?
Central field (T)	1.8	1.5	1.5	2
Inner bore (m)	1.85	4.96	2.8	1.9
Length (m)	2.5	7	3.46	2.7
Energy (MJ)	12.5	137	25	20
Current (A)	5000	5000	7110	5000
Weigth (t)	2.5	60	6.5	5?
Rad. length	0.9	1.6	1.4	0.5?
Cable section (mm)	$4.3 \times 15$	$3.6 \times 35$	$3.2 \times 30$	$3.3 \times 25$
Current density ( $\frac{A}{mm^2}$ )	78	40	74	50

**Table 2:** Comparison of solenoids used in experiments similar to PANDA.

The PANDA detector schedule identifies the magnet as a critical procurement item: the setup of the yoke, cryostat and solenoid is compulsory for the installation of all the active parts of the detector. This is due to the fact that the cryostat itself provides mechanical support for the various detectors: so, before the assembly, also tests and commissioning of the magnet are needed. The solenoid design, fabrication and commissioning duration foreseen is  $30 \div 36$  months, so the contract should be awarded in the summer of 2008 to meet the overall detector schedule.

The magnet cryostat will be designed, fabricated and inspected according to the intent of the ASME Boiler and Pressure-Vessel Code, Section VIII, Division 2 [2], but will not be code-stamped. For steel structures, the allowable design stresses follow the standard guidelines of European and Italian standards [3][4]. Bolted connections and fasteners will conform to their recommended torques and allowable stresses depending on the connection. The flux return is fabricated with S235 JR structural steel plates or a material with similar mechanical and magnetic properties.

## 2.1 Description of Key interfaces

### Superconducting Solenoid and Flux Return.

The radial distance between the outer diameter of the cryostat and the inner surface of the barrel flux return is 100 mm: in this space is foreseen a double layer of muon detectors. The presence of muon chambers inside the

barrel is compulsory to achieve a sufficient tracking capability for low energy muons. The solenoid weight and magnetic forces are transmitted to the yoke by means of titanium and structural steel supports. These attachments, providing also the load path for the inner detector components to the barrel flux return, are described in detail in the next sections.

In the barrel are foreseen different chases for the cryostat chimney and for the target pipe: these chases have proper shapes and dimensions of the order of 20 ÷ 50 cm. The signal cables exit through the upward end doors and through additional rectangular chases between the barrel and the doors.

#### **Barrel and End Doors.**

Both end doors have  $\sim 90\%$  solid steel contact area at the surface with the ends of the barrel. The remaining 10% area of the barrel ends is reserved for cabling and utilities from the inner detector components. The end doors are attached to the barrel with tie plates that are bolted to the end door structure and to the barrel itself.

#### **Particle Identification System.**

The Particle Identification is obtained mainly thanks to a DIRC whose silica stacks are placed between the tracker and the calorimeter. The Čerenkov light produced in the DIRC has to be projected on an array of small PMTs in order to measure the radius of the Čerenkov cone and to reconstruct the particle speed. These PMTs have to be placed outside the yoke in a region with magnetic field less than 10 G. On the other hand, the length of the stacks has to be minimized to reduce light loss and costs. A magnetic shield made of iron and mu-metal is foreseen to achieve the desired field in PMTs region (see fig. 2): the suspension system for the DIRC water vessel and for this shield is not defined yet.

#### **Inner Muon Detector and Solenoid.**

There is a muon counter between the cryostat and the yoke. This detector is directly attached to the barrel, and, with the microvertex detector, which is suspended to the beam pipe, is the only one that doesn't load the cryostat. Because of the presence of the cryostat support, a proper design for the muon plates located inside the barrel is needed.

#### **Movable End Door Skids and the Beam Line.**

The end doors are mounted on skids equipped with rollers so that they can be moved away from the barrel for maintenance access. The end door skids move on tracks installed in the floor. The end doors clear the beam line magnets, vacuum pumps, magnet stands, and other beam line equipment during door opening.

#### **External Platforms, Stairways, and Walkways.**

The external platforms necessary to install and service electronic racks and cryogenic equipment are supported from the flux return. The require-

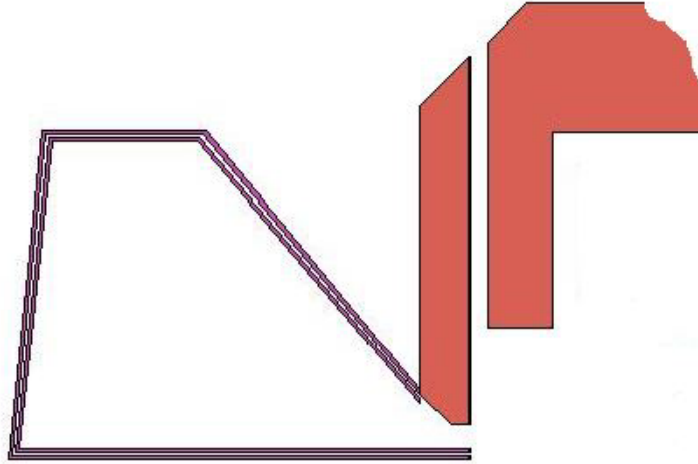


**Figure 2:** The DIRC magnetic shielding.

ments of these components have not yet been determined.

## 3 Summary of Projected Magnet Performance.

### 3.1 Central Field Magnitude and Coil Performance.

The magnetic field of 2 T is obtained by energizing the solenoid with a constant current of 5000 A. The conductor is operated at 50% of the critical current, with a peak field in the conductor of 2.8 T. This gives a large safety margin.

Magnetic uniformity is achieved by using different current densities in regions at both ends of the solenoid w.r.t. the central region. This is done by adding more aluminum stabilizer to the central region conductor, which reduces the current density there. Fig. 3 shows the field uniformity in the central region. The areas in which the field nonuniformity is greater than 1.5% are small and are located in regions in which they do not affect the performance of the drift chamber. In addition, once the solenoid parameters are optimized, the corners of the drift chamber are also within  $\pm 2\%$  of 2 T.

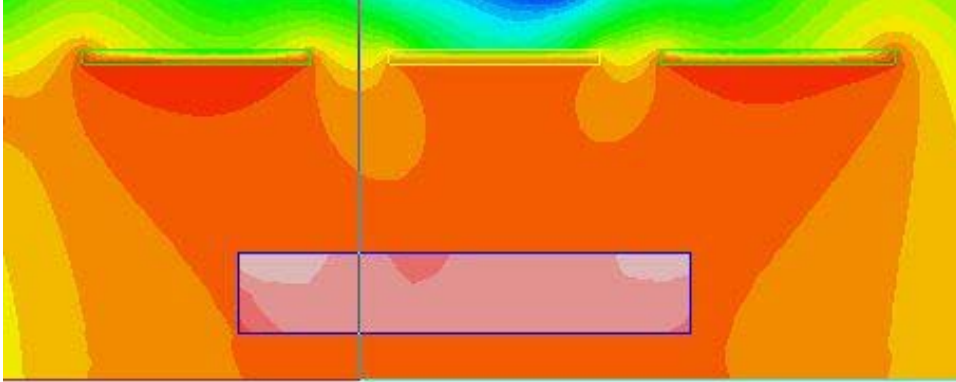


**Figure 3:** Field uniformity inside the solenoid: in pink the outer tracker region (division is 1%).

The radial pressure due to magnetic forces on the conductor during operation is  $\sim 2.90$  MPa in the high current density regions and  $\sim 1$  MPa in the central region of the conductor. An aluminum alloy support cylinder surrounds the coiled conductor to react against these radial pressures and keep the conductor from yielding.

The integrated axial force on the winding is  $\sim 8$  MN. The conductor winding and support cylinder are mechanically coupled by an epoxy bond. This epoxy bond allows some of the axial load to be transmitted in shear to the outer aluminum cylinder, which keeps the conductor from yielding. There is an axial  $\sim 1$  MN decentering force applied to the conductor winding due to the asymmetry in the iron yoke.

### 3.2 Flux Return

The flux return assembly provides an external flux path for the magnetic field of the superconducting solenoid. Fig. 4 shows the flux lines from the magnetic analysis. There are large body forces acting on the coils and on the end doors as a result of the magnetic field.

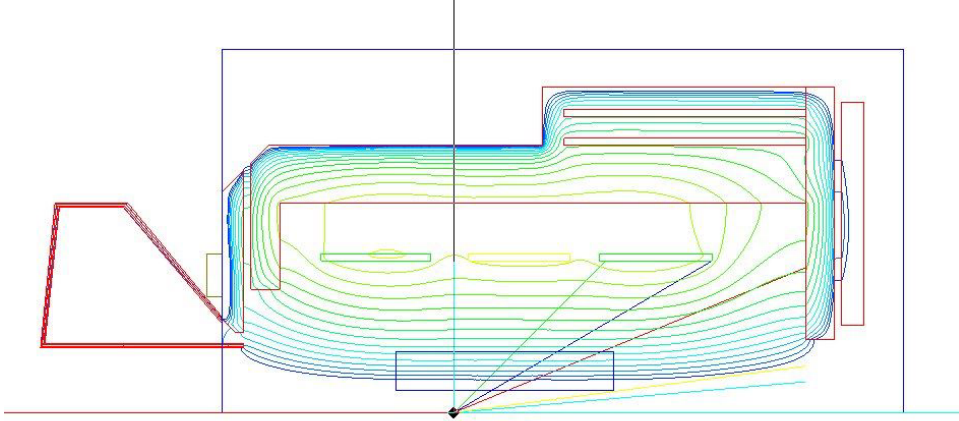


**Figure 4:** Flux lines all over the detector.

## 4 Superconducting Solenoid.

### 4.1 Magnetic Design.

This section describes the main features of the superconducting solenoid. A cross section of the solenoid is shown in fig. 5, and parameters are given in table 3.

The magnetic analysis is based on a two-dimensional axially symmetric model and on a complete three-dimensional model. These models include the solenoid, flux return yoke, shields, some ancillary equipments and end doors.

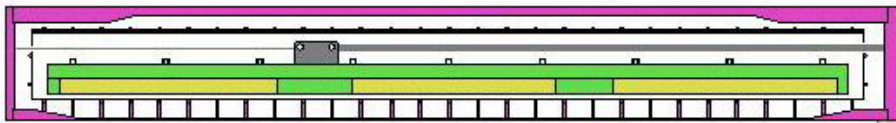


**Figure 5:** Coil schematics: in purple the cryostat, in green the coil former, in yellow the windings.

The backward shield is designed to accommodate the DIRC. Its main functions are to improve the field uniformity in the backward region of the outer tracker and to balance the magnetic force on the solenoid due to the yoke asymmetry. A detailed design of this shield is underway. The iron prop-

erties used for computation ([5] two-dimensional magnetic element) are those of hot-rolled carbon steel.

The magnet design provides a magnetic field of 2 T with a uniformity of  $\pm 2\%$  in the tracking region. This is obtained by grading the current density of the solenoid in three regions connected in series. The central region is 700 mm in length with 133 turns. Two end regions are 755 mm and 780 mm in length with 216 and 223 turns respectively. The current density in the end regions is 1.5 times that of the central part. A better field uniformity may be obtained by reducing the axial length of the two end regions and increasing the current to generate the same field, but this would cause a reduction in stability against thermal disturbance. For the initial design, the maximum allowed current density in the conductor has been limited to the maximum currently attainable for magnets of this kind, i.e., 80 A/mm<sup>2</sup> (ZEUS magnet). In these conditions, a cross section of 80 mm<sup>2</sup> for the smaller conductor corresponds to a maximum current of  $\sim 6400$  A: our choice of 5000 A gives a good margin for operations.

Parameter	Value
Central Induction	2 T
Conductor Peak Field	2.8 T
Uniformity in the Tracking Region	$\pm 2\%$
Winding Length	2.7 m
Winding Mean Radius	1070 mm
Amp Turns	$5.86 \cdot 10^6$
Operating Current	5000 A
Inductance	1.6 H
Stored Energy	20 MJ
Total Length of Conductor	8000 m

**Table 3:** The main parameters of the winding of the PANDA solenoid.

Fig. 6 shows the graph of the field strength over the full detector region. The magnetic field is essentially symmetric: in addition, a field uniformity better than  $\pm 2\%$  is obtained in the inner and outer tracker regions. Field uniformity is required up to  $z = 1100$  mm in the forward region, and the present design provides a uniform field up to  $z = 1200$  mm, providing a factor of safety. Further adjustment of the backward shield geometry may improve field quality, in the sense of an improvement of the field uniformity in the backward region.

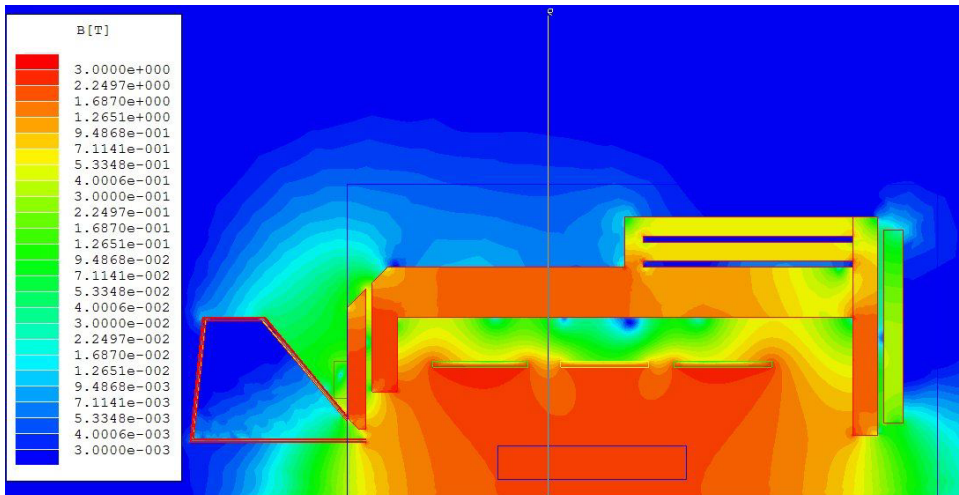


**Figure 6:** The field strength over the full detector region.

## 4.2 Cold Mass Design.

### Aluminum Stabilized Conductor.

The conductor is composed of a superconducting Rutherford cable embedded in a very pure aluminum matrix by a coextrusion process that ensures a good bond between aluminum and superconductor. Table 4 shows the main parameters of the conductor<sup>2</sup>.

The operating current for this conductor is 50% of the critical current at twice the peak field, giving a large safety margin. In the case of local heating up to 5.2 K, there is still a significant margin on the critical current ( $I = 0.6I_c$ ). At 2.8 T, the conductor critical temperature is  $T_c = 8.15$  K, and the current sharing temperature is 6.3 K. This values can be calculated using the Lubell Formulas[6]:

$$T_c(B) = 9.25 \text{ K} \left( 1 - \frac{B[\text{T}]}{14.5 \text{ T}} \right)^{0.59}$$

which describes the critical temperature as a function of the magnetic field on the conductor and

$$J_c(B) = J_0 \left( 1 - \frac{T}{T_c(B)} \right)$$

---

<sup>2</sup>A more extensive description of the thermal and mechanical issues of this project is presented in Andrea Pastorino's paper.

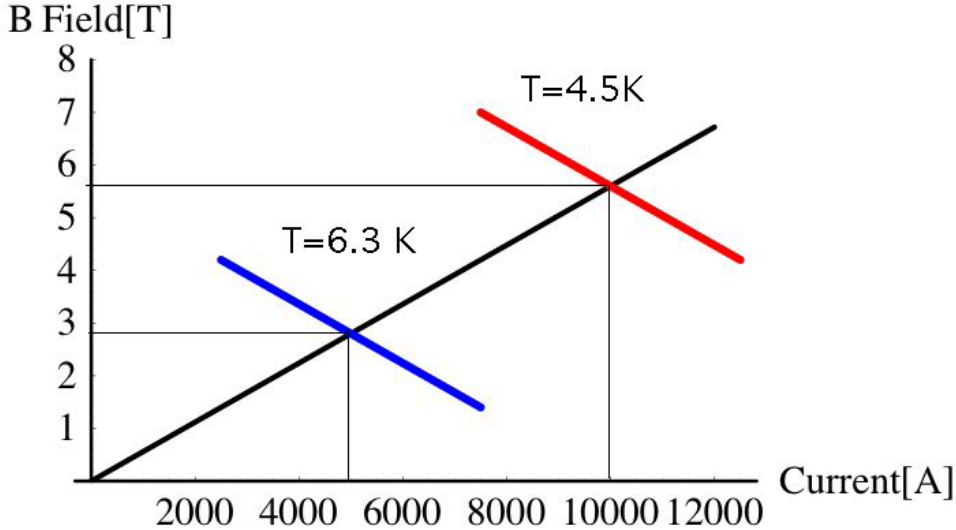


**Figure 7:** Superconducting cable work point calculation. The red line represents the current sharing vs. magnetic field curve at 4.5 K calculated for our cable: the cable was chosen to be critical at twice the current and twice the magnetic field w.r.t. the work ones. The blue line represents the sharing current vs. magnetic field at the work condition ( $I = 5000$  A,  $B = 2.8$  T): the sharing current temperature is here 6.3 K, giving us a safety margin  $\Delta T = 1.8$  K.

which describes the critical current density as a function of the magnetic field on the conductor and of the temperature.

A simple method to evaluate the stability of the winding consists of considering the enthalpy margin per unit length between the operating and the sharing temperature. This stability parameter for the PANDA solenoid is 0.5 J/m, which is the same value obtained for the ALEPH and BaBar magnets.

The cross section of the conductor is  $3.3 \times 24.6$  mm<sup>2</sup> for the higher current density regions and  $5.15 \times 24.6$  mm<sup>2</sup> for the central region. The coil winding can be made using six 1500 m lengths of conductor, requiring five electrical joints. Each joint, made by either by TIG welding (as in the Atlas barrel Toroid and CMS), or soft soldering (after electro-deposition of copper) a suitable length of the aluminum matrix must have a resistance less than  $5 \cdot 10^{-10}$   $\Omega$ , limiting the power dissipation to a few milliwatts.

### Winding Support

The winding will be supported by an external aluminum alloy cylinder

similar to other existing detector magnets. The winding support is designed for all aspects of force containment, i.e., its weight and the radial and axial magnetic forces. Fig. 8 shows these magnetic forces on the solenoid.

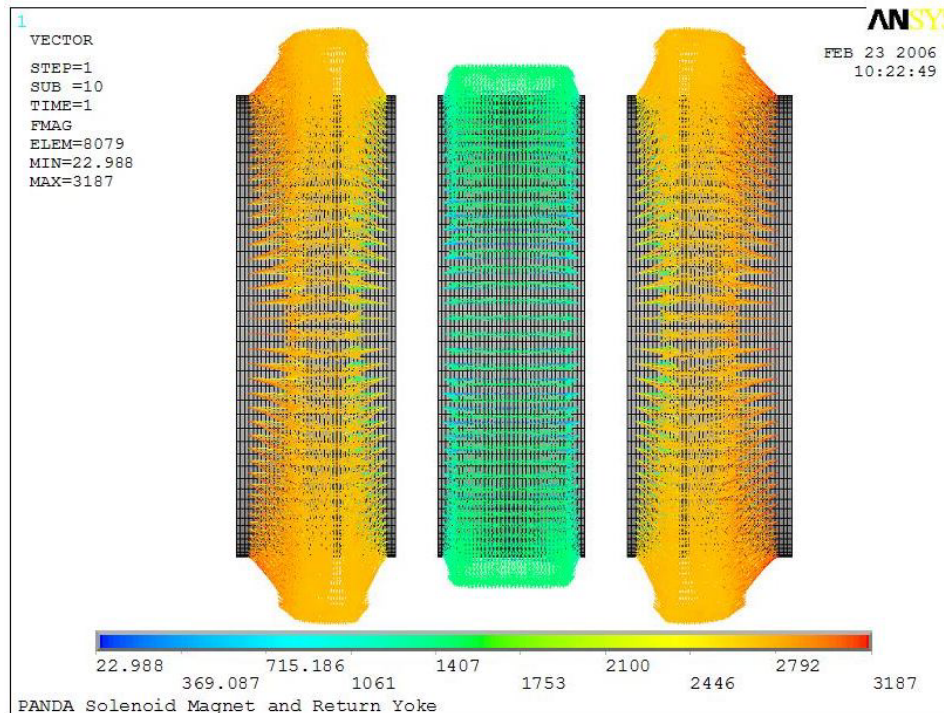


**Figure 8:** The force distribution on the coils (beam direction is left-to-right).

The maximum radial pressure,  $\sim 2.90$  MPa, is generated in the high current density regions at the ends of the coils. A pressure of  $\sim 1$  MPa is generated in the central region. An aluminum alloy (Al 5083 T0) support cylinder surrounds the coiled conductor to react against these radial pressures and prevent coil movement. An extended stress analysis of the solenoid coil-support cylinder assembly has been developed to investigate the behaviour of the high-ductility pure aluminium stabilizer and epoxy resin under the high radial pressures generated by magnetic forces. The cable was thus simulated including the material non-linear stress-strain curve. As a result, plastic deformations are expected to occur in the coils during the first charge. The amount of these deformations is small and ensures that the cable will not be stressed beyond the elastic limit in the subsequent charges. This will help prevent premature quenching during coil energizing. Nevertheless, the support cylinder is capable to contain the deformations of the coils while remaining

in the elastic field.

Parameter	Value
Conductor Type	NbTi Pure Al-stabilized Co-extruded
Aluminum RRR	> 500
Conductor Unit Length	1.5 km
Number of Lengths	6
Bare dimensions	3.3 and $5.15 \times 24.6 \text{ mm}^2$
Insulated dimensions	3.7 and $5.55 \times 25 \text{ mm}^2$
Superconducting Cable	Rutherford type
Dimensions	$9 \times 1.23 \text{ mm}^2$
Strands Diameter	0.84 mm
Number of Strands	20
Cu/Sc	1.8
Filament Diameter	$20 \mu\text{m}$
$I_c(B = 2.5 \text{ T}, T = 4.5 \text{ K})$	> 10 kA
Insulation Type	Fiberglass Tape
Insulation Thickness	0.4 mm

**Table 4:** Conductor parameters.

An integrated compressive axial force of  $\sim 8 \text{ MN}$  is induced in the winding. The distribution of the axial force within the coil is complex. The central part is slightly axially stressed by a force of less than 1 MN. For preliminary calculations of the axial stress, the maximum force was considered (4.3 MN in the worst case for one of the three coils). This would lead to an axial stress of 13 MPa on the pure aluminum, with only the winding supporting the axial forces. However, if the axial force is transmitted to the outer cylinder, the stress is considerably lowered. In this case, the shear stress between the winding and outer supporting cylinder is less than 3 MPa. This low value of shear stress will allow the winding and support cylinder to be mechanically coupled through an epoxy impregnation without applying any axial prestress to the winding (as was done for the ZEUS and BaBar magnets). Epoxy impregnation can support a shear stress higher than 30 MPa, providing a high safety margin. This leads to a simplification and cost saving in the winding fabrication.

The current design causes axial decentering forces on the coil due to the iron asymmetry and a residual force of 1 MN is applied to the winding. A

more careful design of the backward shield can help reduce the amount of this residual axial force by some 10%: nevertheless, this force has to be supported by specifically designed and calculated structures. For this purpose, 8 axial bars, made of high-resistance Titanium alloy, have been foreseen, together with 16 radial bars, which account for the weight of the barrel and possible forces due to a misalignment of the assembly with respect to the central axis.

While the preliminary analyses described above decoupled the effects of radial and axial magnetic forces on the coils and support cylinder, a comprehensive 3D FEM analysis has been made simulating the coil and cylinder assembly under the effect of the magnetic field during nominal operations. The results of this calculation (see Fig. 9), confirming previous analyses, are pointed out below:

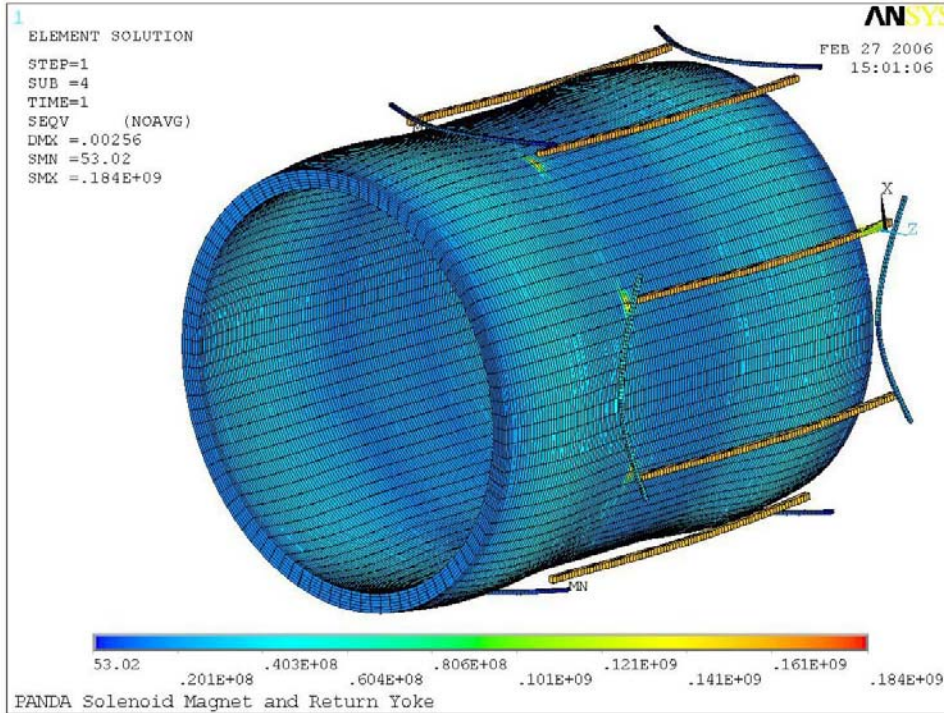
- The radial pressure generated in the windings causes the pure aluminium stabilizer to exceed its elastic limit, showing permanent deformations after the first charge. Nevertheless, the amount of the plastic deformations is negligible and stresses will remain within the elastic range during the subsequent charges.
- The shear stress transmitted through the epoxy resin to the aluminium support cylinder is fairly low if compared to the resin capabilities.
- Stability of the whole assembly is ensured by the Al 5083 aluminium barrel. The analysis show that the cylinder is capable to contain the radial and axial deformations of the windings without showing permanent deformations.
- Axial and radial supports have also been included in the model. The decentering forces caused by the asymmetry of the return flux and the weight of the assembly are well supported by the suspension system, the stresses calculated for the bars being well below the elastic limit for Titanium alloys (Ti 6Al 4V or Ti 5Al 2.5Sn).

Table 5 shows the main features of the cold mass. The values are given at a temperature of 4.2 K. The dimensions at room temperature are higher by a factor of approximately 1.004.

### **Electrical Insulation**

Electrical insulation is an important aspect of solenoid design and manufacture. Two categories of insulation are required: ground plane insulation between the coil and support cylinder, and turn-to-turn insulation.

- The ground plane insulation must operate at relatively high voltages during quench conditions and will be subjected to strict QA controls.



**Figure 9:** Stress on solenoid coil, barrel and supports.

The design of the quench protection systems is based on a maximum voltage to ground of 500 V. The ground plane insulation will be made by a 0.8 mm layer of fiberglass cloth inserted between the support cylinder and the solenoid outer layer during the winding. Summing up this insulation layer to the cable insulation we get a ground insulation of  $\sim 1$  mm. We are confident from the previous experience on similar solenoids (BaBar, Zeus, CMS) that this ground insulation thickness should be adequate to withstand the quench voltage of  $\sim 500$  V. The insulation will be fully tested at 2 kV along the winding process. At the end of the ground plane insulation will be fully vacuum impregnated with high strength epoxy resin.

- The conductor will be insulated with a double wrap of 0.125 mm glass tape during winding to give an insulation thickness of 0.2 mm (80% compacted). The resulting turn-to-turn insulation thickness will be 0.4 mm and will be fully impregnated in the bonding process. Electrical tests will be carried out during winding to detect any failure of insulation. The tests will include regular/continuous testing for turn-

to–turn and turn–to–ground insulation.

### 4.3 Quench Protection and Stability.

#### Protection Concept.

The solenoid will be protected by an external dump resistor which will determine the current decay under quench conditions and allow extraction of 75% of the stored magnetic energy. The quench protection concept is shown in fig. 10, and quench parameters are given in table 6. The protection concept is based on two main criteria.

Since the calculated stored energy for the magnet is  $\sim 20$  MJ at an operating current of 5000 A, an inductance of 1.6 H is expected. To have a sufficiently fast and effective quench spreading and energy extracion, a  $0.1 \Omega$  was chosen. The time constant of this circuit during a fast discharge is so 16 s.

- A voltage limit of 500 V across the solenoid applies during fast discharge. Centertapping of the fast dump resistor to ground will limit the voltage to ground to 250 V. The center–tapped resistor will also allow the measurement of ground leakage currents as a safety and diagnostic tool.
- An upper temperature limit of 100 K applies during quench conditions. This limit will give very good safety margins against peak temperature rise and thermally induced stresses at quench.

#### Quench Analysis

A preliminary quench analysis of the PANDA solenoid has been made using a code developed for indirectly cooled solenoid design. The code models the thermal and inductive behavior of the solenoid in order to account for quench–back effects and heat transfer to the support cylinder. This analysis shows that quench–back is predicted about two seconds after opening the protection circuit breakers.

Several different calculations were performed (courtesy AS-G Superconductors, formerly known as Ansaldo superconductors), simulating a local temperature rise in different locations on the coil. It was seen that the worst situation is encountered when he quench is generated in the downstream, internal coil. The temperature of the various windings<sup>3</sup> are reported in fig. 11: never in any simulation the temperature on the superconducting cable

---

<sup>3</sup>The coils are numbered this way: 1. external upstream; 2. external central; 3. external downstream; 4. internal downstream; 5. internal central; 6. internal upstream.

Parameter	Value
<b>Winding:</b>	
ID	2090 mm
OD	2190 mm
Length	2695 mm
Weight	2.0 t
<b>Supporting Cylinder:</b>	
Material	Al alloy 5083
ID	2190 mm
OD	2290 mm
Length	2775 mm
Weight	3.1 t
<b>Ground Insulation:</b>	
Material	Fiberglass epoxy
Thickness	0.8 mm
Total Solenoid Weight:	5.1 t
<b>Nuclear Interaction Length: (Assuming Aluminum)</b>	
Maximum	$0.2 \lambda_{\text{int}}$
Minimum	$0.15 \lambda_{\text{int}}$

**Table 5:** Cold mass (4.5 K) parameters.

exceeded 65 K, and in every situation the temperature, after a short period, drops to  $\sim 40$  K.

The role of the coil former as a quench spreader has been studied comparing the temperature rise with and without the coil former itself: this case is similar to the one of a coil former made of a poor heat and current conductor, such as stainless steel, carbon fibre or similar. Even in this configuration, the quench remains limited to the coil in which is started and in the closest one, and the temperature doesn't exceeds 80 K.

Fig. 12 shows the voltage at the ends of each winding and the current in the coil after a quench: a time constant of  $\sim 16$  s is obtained, confirming the value of inductance of  $\sim 1.6$  H obtained from pure magnetic calculations.

### **Stability.**

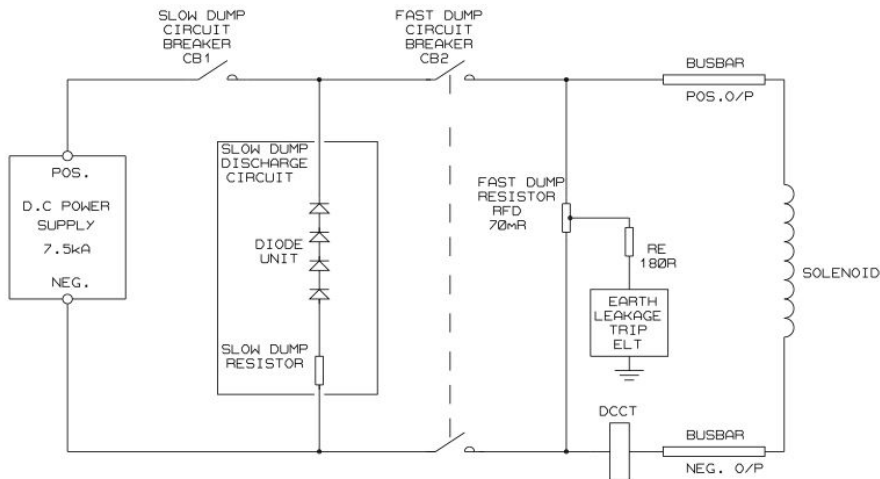


**Figure 10:** Solenoid power and quench protection concept.

The PANDA solenoid coil will be indirectly cooled using the technology established for existing detector magnets such as DELPHI and ALEPH. The reliable operation of those magnets has demonstrated that safe stability margins can be achieved using high-purity, aluminum-clad superconductors in a fully bonded, indirectly cooled coil structure.

Conductor stability has been estimated using an analysis code in order to establish the minimum quench energy ( $MQE$ ) for transient heat pulses. The computed  $MQE = 1.4$  J. The computed minimum quench length ( $MQZ$ ) is 0.6 m.

These margins are considered to be safe for the PANDA solenoid due to its low-stress design. The stability margin will be optimized during the full design study.

## 4.4 Cold Mass Cooling.

### Cooldown.

Cold mass cooldown is accomplished by circulating cold helium gas either directly from the refrigerator or from a storage dewar with gas mixing.

### Operating Conditions.

Under operating conditions, the cold mass is cooled by circulating two-phase helium in pipelines welded on the coil support cylinder. The cooling circuit will be driven either by forced or natural (thermo-syphon) convection.

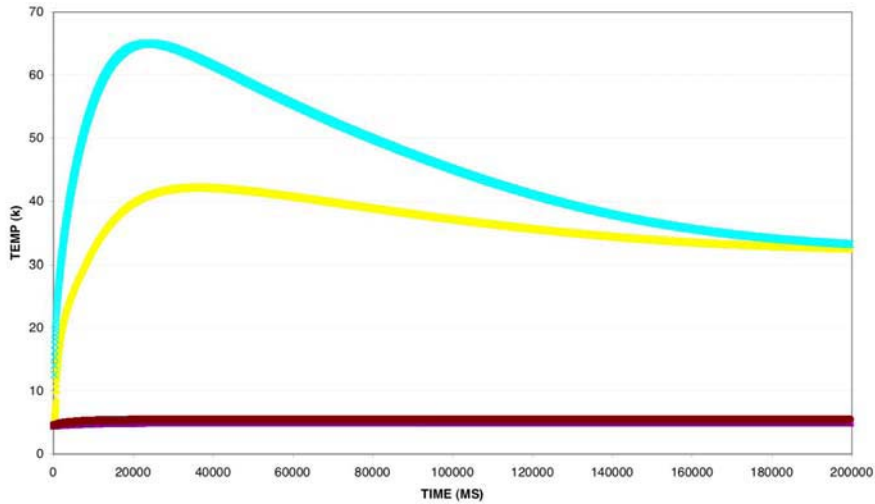


**Figure 11:** Temperature after a quench as a function of time for the 6 windings in the worst situation (courtesy AS-G Superconductors).

This technology is established and yields the simplest operational mode. The thermo-syphon cooling circuit is designed for high flow rates to ensure the correct quality factor for the helium. The circuit is fed through a manifold at the bottom of the support cylinder. The cooling circuits are welded to the support cylinder surface with a spacing of  $\sim 0.3$  m to limit the temperature rise. The cooling pipes terminate in an upper manifold. The circuit will be designed to provide operation during quench conditions. In order to confirm these assumptions, a finite element model of  $1/8$  (thanks to the axial symmetry) of the coil-barrel has been developed. With the estimated static heat loads (reported in the next paragraph), a pipe diameter equal to 20 mm and a liquid helium mass flow of 28 g/s, the maximum temperature rise is equal to 0.31 K with reference to the design temperature of 4.5 K (see Fig. 14). The conceptual layout of the cold mass cooling circuit (forced convection solution) is shown in fig. 13.

### Heat Loads.

The estimated static heat loads for the solenoid are given in table 5. Eddy current heating in the support cylinder will cause additional heat loads during charging of the solenoid. However, for a solenoid charging time of 30 min, the estimated transient power is 8 W, which is small compared to static heat loads.

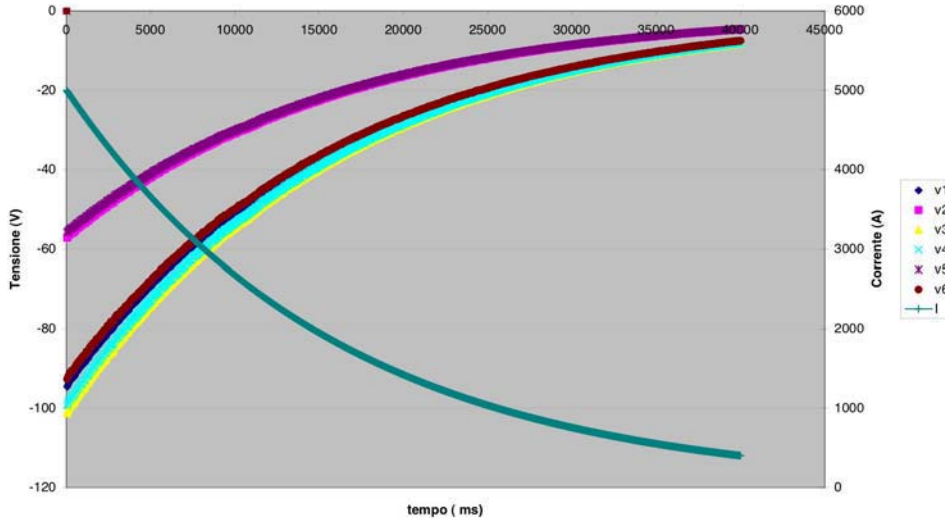


**Figure 12:** Voltage and current after a quench as a function of time for the 6 windings (courtesy AS-G Superconductors).

## 4.5 Cryostat Design.

### Vacuum Vessel.

The cryostat consists of an annular vacuum vessel equipped with radiation shields and superinsulation. The vacuum vessel is designed to satisfy a number of basic criteria:

1. Support vacuum loads in accordance with recognized pressure vessel codes;
2. Carry the cold mass and radiation shield weight through the insulating supports;
3. Support magnetic loads (107 metric tons of axial forces) during nominal operations;
4. Operate with deflections of less than 1 mm under all loads when mounted in the flux return barrel;
5. Carry the weight of the inner detectors (The calorimeter actual weight is 18 metric tons. The calculation has been made with a magnifying factor of 1.15);

The vacuum vessel is designed as two concentric cylinders with thick annular end plates, all of aluminum alloy 5083; its basic parameters are given in

Parameter	Value
Operating Current	5000 A
Stored Energy	20 MJ
Inductance	1.6 H
Quench Voltage	500 V
Protection Resistor	0.1 $\Omega$
Time Constant	$\sim 15$ s
Adiabatic Peak Temperature	100 K
Overall Current Density: Conductor 1	54 A/mm <sup>2</sup>
Conductor 2	36 A/mm <sup>2</sup>
Aluminum Stabilizer RRR Zero Field	1000

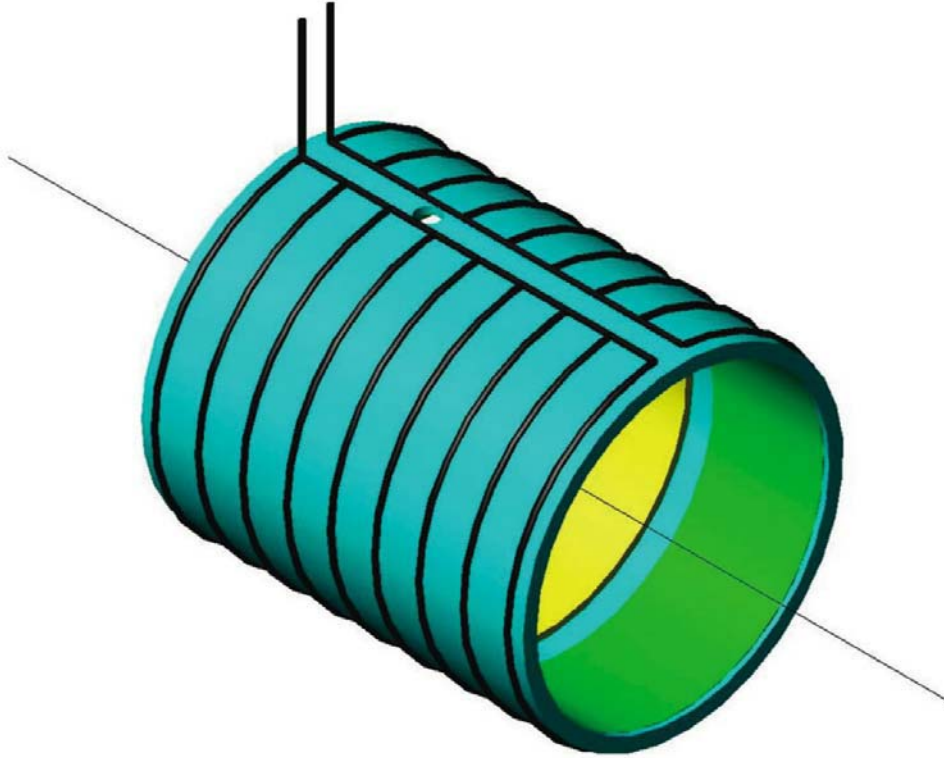
**Table 6:** Quench parameters.

table 8. The minimum thickness of the different parts composing the cryostat are calculated according to ASME Code for Pressure Vessels. A preliminary finite element (FE) structural analysis of the vessel has confirmed that design criteria (1)÷(4) can be met with reasonable safety factors. Maximum vessel deflections are less than 1 mm, and stress levels peak up to 70 MPa with all loads applied (see Fig. 15). The cryostat can also be made of AISI 304 Stainless Steel; in this case, a decrease of deformability and an increase of stress level is expected.

**Thermal Shielding.** The cryostat is equipped with radiation shields, which operate at 40–80 K, and superinsulation. The shields are cooled by helium gas supplied directly from the refrigerator. About 30 layers of superinsulation separate the vacuum vessel walls from the radiation shields. Another five layers will be installed between the shields.

**Services.** Cryogenic supplies and current supplies are connected from a services turret to the cryostat through the service chimney in the backward end door. Current leads and local control valves are mounted in the services turret.

We foresee to use standard copper counterflow cryogenic current leads rated to the running current of the magnet: this means a LHe consumption of 171/h. Cryogenic relief valves are also mounted in the service turret for quench and refrigeration failure conditions.



**Figure 13:** Cold mass cooling circuit. The cryogenic supply chimney passes through a cutout in the backward end of the barrel flux return.

## 4.6 Coil Assembly and Transportation.

The coil will be assembled inside the cryostat at the manufacturer's plant. Electrical and cryogen connections will be made at the chimney so that the coil can be tested before shipping.

A complete cooldown will be carried out from room temperature to the operating temperature of 4.5 K. The cooldown will allow checking of cooling time, temperature control, heat loads, and full operation of sensors. A magnetic test will also be performed at low field (30% of the operating current) to check superconductor operation, the joint resistance, and the additional losses due to the eddy currents in the outer structural cylinder at the coil ramp-up.

Before delivering the magnet, but after the tests at the factory, the end flanges will be dismantled to allow a hard connection of the cold mass to the cryostat walls. Depending on the transport facilities, the cryogenic chimney may also be dismantled. In this case, the electrical and cryogen connections

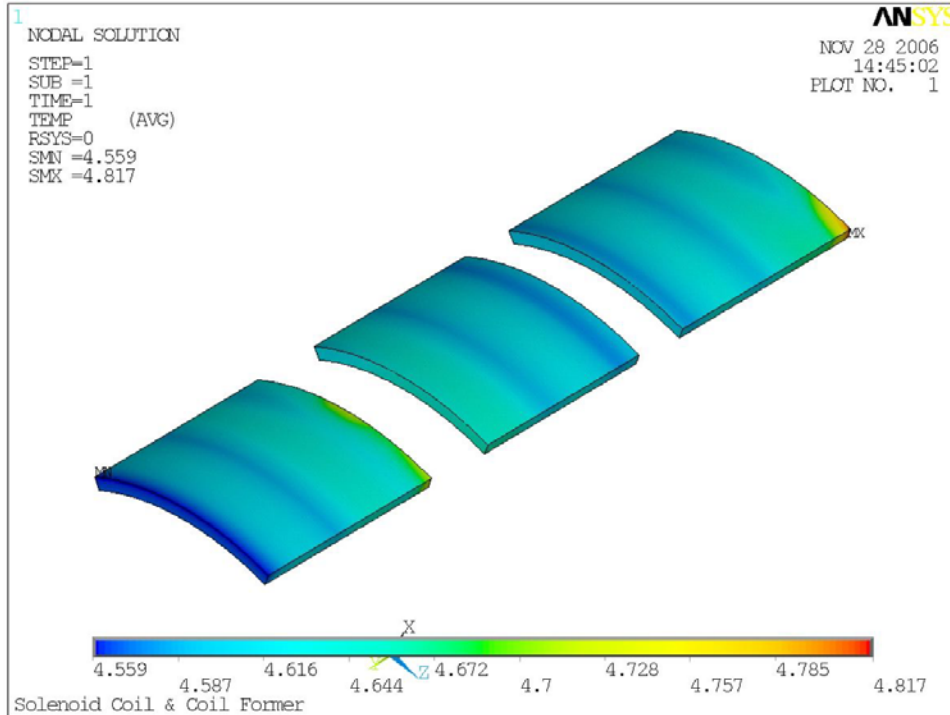


**Figure 14:** Cold mass cooling circuit. Temperature distribution in one eighth of the assembly - nominal condition.

also must be dismantled and protected against breakage.

## 5 Cryogenic Supply System and Instrumentation.

Operation of the superconducting solenoid requires both liquid helium and cold helium gas (20 K  $\rightarrow$  100 K) for cooldown and refrigeration of the thermal shields. Similar systems have been used successfully throughout the HEP community. A summary of the cryogenic loads is given in Table 7.

The solenoid is equipped with a full set of instrumentation sensors for monitoring, control, and diagnostic purposes. Instrumentation includes temperature sensors for the cold mass, shield cryogen flow monitoring, and strain gauges in the coil support cylinder. Voltage taps monitor the electrical resistance of the conductor joints and quench detection. The quench detection systems are hardwired to interlocks. The solenoid instrumentation and controls are integrated with the BABAR experiment and refrigeration controls.

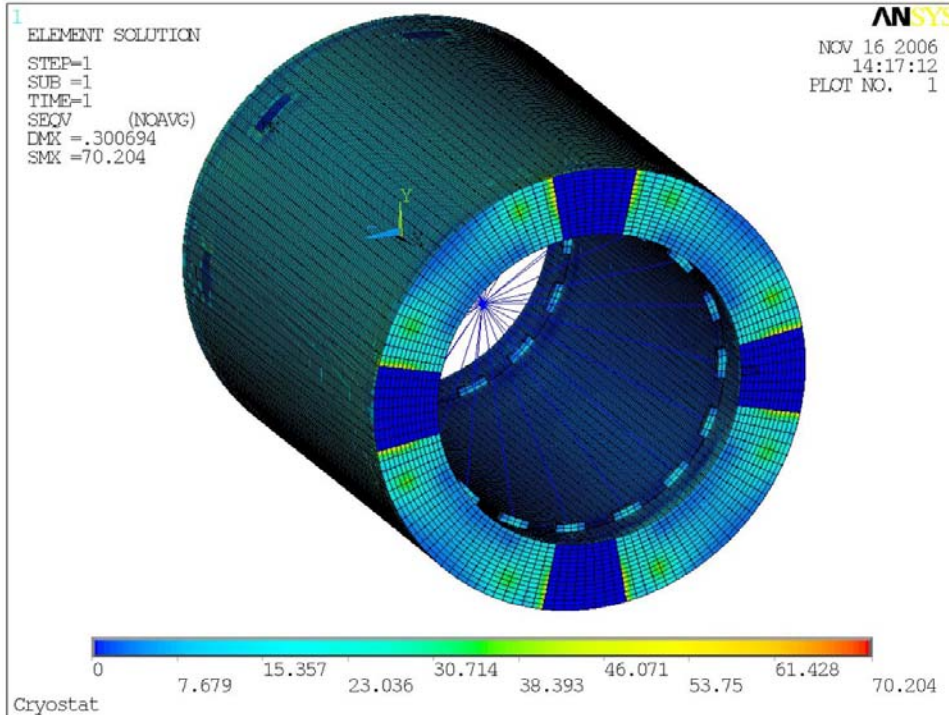


**Figure 15:** Vacuum Vessel FEM model, equivalent stress with all loads applied.

The liquid helium plant, which is fully automatic, is furnished with a process control system and all requisite logic and software necessary for all operational modes. Control and monitoring of the cryogenic plant and the magnet coil, together with remote control and monitoring of the compressor room, is carried out from a control room adjacent to the plant room. Main operating parameters are interfaced with the PANDA data acquisition and monitoring systems.

## 6 Flux Return.

### 6.1 Overview.

The flux return assembly provides the external flux path for the magnetic field from the superconducting solenoid. The flux return also provides the gravitational and seismic load path for the barrel detector components to the concrete foundation.

The flux return assembly consists of a barrel, four external support legs,

Magnet Heat Loads at 4.2K	
Item Parameter	Load
Cold Mass	5000 kg
Total Surface Area	44 m <sup>2</sup>
Radiation Heat Flux (Design)	0.07 W/m <sup>2</sup>
Radiation Heat Load (Design)	3.1 W
Conduction Heat Load	2.2 W
Cable Joints	max 2 W
Cryogenic Chimney	10 W
Gas Load	1 W
Eddy Currents (1500 s ramp time)	10 W
Total 4.5 K (SF of 2)	57 W

Magnet Shield Heat Loads at 60K	
Item Parameter	Load
Shield Mass	1000 kg
Total Surface Area	44 m <sup>2</sup>
Radiation Heat Flux (Design)	1.3 W/m <sup>2</sup>
Radiation Heat Load (Design)	57 W
Conduction Through Supports	17 W
Conduction To Shields <sup>4</sup>	150 W
Diagnostic Wires	1 W
Gas Load	2 W
Eddy Currents (1500 s ramp time)	10 W
Total 60 K	237 W

**Table 7:** Cryogenic heat loads.

two sets of end doors, roller mechanisms, and vertical adjustment systems. The design of the flux return and its components reflects the limitations of the experimental hall.

End door components must be movable once the detector is assembled to allow maintenance access to inner detector subsystems. The design of the flux return provides a means for proper alignment of all flux return components with respect to the detector magnet and the beam line. This alignment must be reestablished after maintenance is performed.

#### **Analysis of the Flux Return.**

The flux return analysis will investigate the overall structural integrity, including that of the supporting structures. This includes looking at all the

Envelope Dimensions	
Inner Radius	950 mm
Outer Radius	1340 mm
Length	3100 mm
Inner Cylinder Thickness	10 mm
Outer Cylinder Thickness	30 mm
Annular End Plates Thickness	50 mm
Materials	AL5083, AISI 304

Design Loads	
Vessel Weight	6 t
Cold Mass	5 t
Calorimeter	18 t
Other Detectors	3 t

**Table 8:** Vacuum vessel parameters.

components and connections involved in the operation, assembly, and seismic loadings of the structure. Operating loads for the barrel include both the gravitational and the magnetic forces. Assembly loads include any additional fixture weights that need to be attached during assembly.

## 6.2 Barrel Flux Return Description.

The barrel flux return assembly extends 4050 mm in  $z$ , and the center is positioned 650 mm from the interaction point in the positive  $z$  direction. The barrel flux return extends radially from the detector axis from 1440 mm to 1840 mm and consists of 8 equal sectors that form an octagonal shape. The sectors consist of blocks with multiple steel plates oriented parallel to the axis of the solenoid.

The inner and outer parallel plates of each block are welded into a rigid superlayer using full penetration welds along their entire thickness in the radial direction (perpendicular to the beam line). The sectors are kept in place with a system of welds and supports that makes the whole barrel sufficiently rigid to keep all the magnetic and gravitational forces. The structure foreseen to host the muon chambers is mounted independently with the same technique.

The use of double block construction for each of the octagonal sectors of the barrel flux return isn't sufficient to provide a significant safety margin

with respect to the 25 t rated capacity of the overhead crane in experimental hall. To mount the barrel, a dedicated machinery from the outside will be used. The weight of the barrel flux return is 180 t excluding the external support legs.

#### **Muon chambers structure.**

In downstream direction several layers of muon detectors are foreseen. The first double-layer will be mounted between the outer surface of the cryostat and the inner surface of the barrel, starting at  $z = 750$  mm w.r.t. the interaction point. The presence of this element is needed to achieve a rough tracking of low energy muons: on the other hand, this imposes a gap between the cryostat and the barrel and so additional radial supports are needed.

An “E” structure is foreseen outside the barrel, made of the same steel of the barrel itself, to contain two single-layer muon detectors see fig. 16). Another double-layer will be mounted outside this structure. The steel act as a stopper for the muons and the magnetic field causes a deflection of the tracks, so a certain energy sensitivity can be achieved even with a so small number of active elements.

#### **External Support Legs.**

Two external support leg assemblies provide the gravitational and seismic load path from the barrel flux return to the concrete foundation. Each assembly consists of two legs positioned 3200 mm apart in  $z$ . The legs are fabricated from 30 mm-thick structural steel plates.

Included at each support leg is a 100 t capacity roller and a 150 t capacity jack. A preformed fabric pad is positioned between the jack and the roller to add compliance to the system. The horizontal spacing of the jack and roller assemblies is nominally 5000 mm. Each support leg is approximately 2750 mm in length, 1400 mm in width, and 2000 mm in height. The weight of each support leg assembly is approximately 20 t.

### **6.3 End Door Description.**

The forward and backward end doors are an array of steel plates that form a regular octagon with a central round hole. Both in upstream and downstream direction the end caps are vertically divided in two halves and can be open to let people operate inside the barrel.

Each end door is mounted on a skid that permits it to be raised onto high load capacity rollers by hydraulic jacks and to be moved on tracks located in the experimental hall. This provides a means to move the end doors into proper alignment with the barrel prior to being bolted in place, and to be moved away from the barrel for maintenance access to the detector. The

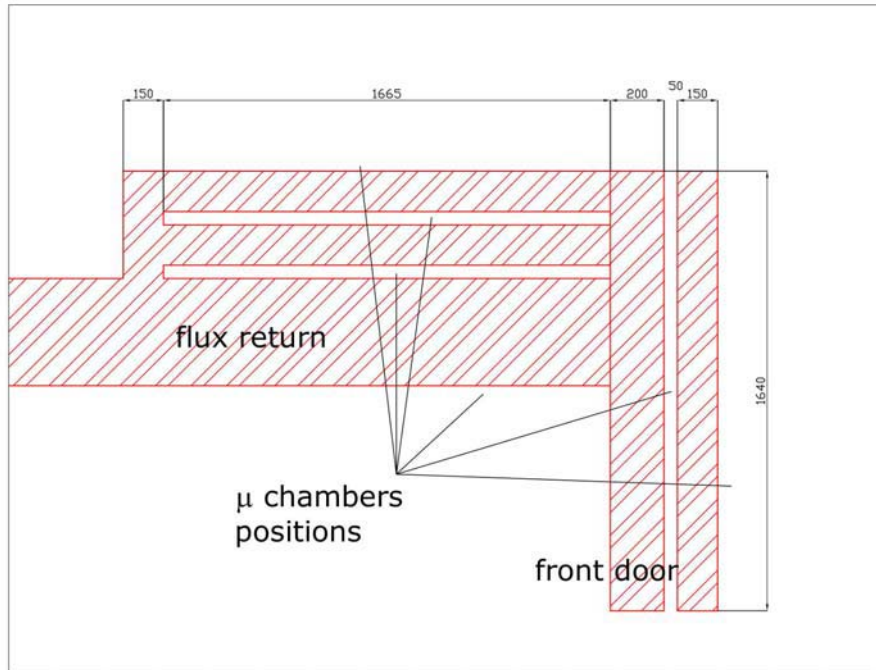


**Figure 16:** Particular of the muon housings in the flux return yoke.

center of gravity of the end door plates is high compared to the depth of the base. The skid provides additional stability during the horizontal accelerations experienced during moving or seismic events.

During operation, the magnet exerts an inward axial force that causes a significant bending moment on the end door plates. The downstream end doors also support the weight of the shielding screen of the dipole magnet and carry the axial magnetic load induced in the plug. To resist gravitational and seismic loads, and to limit the plate stresses and deflections, all the end door plates are joined together to form a single structural member.

The design of the end doors permits each door to be assembled and disassembled inside the experimental hall with the existing facility crane. Each end door is therefore composed of two weldments that are fastened together at installation. The inner weldment consists of four 50 mm plates, with each plate welded to a channel-shaped frame that extends along the top and bottom of the octagon shape and along the boundary between the right and left doors. Additional stiffeners are required to stiffen the weldment and help maintain the necessary gap for the muon chambers. The outer weldment con-

sists of three 50 mm plates welded together with similar stiffening members. The detailed analysis of the response of the plates to the magnetic force distribution is not yet available, nor has a detailed seismic analysis been done for the end door plates. Several design options are being studied that can provide the necessary strength and stiffness.

The inner and outer weldments are joined together at installation by bolting each weldment to the top of the skid along the bottom of the octagon, and by bolting tie plates around the remaining perimeter of the weldments, except where the shielding plugs are located. The outside tie plates are bolted in place after the muon chambers are installed, and provisions for cabling are provided in these outside plates. These tie plates are also used to attach the end doors to the barrel of the flux return.

In upstream direction, the diameter of the hole is fixed by the radius of the DIRC used for PID: its design radius is  $550 \div 600$  mm, so the hole radius is 700 mm, in order to house the trimming coil used to reduce the stray magnetic field in the DIRC PMT region. The end cap has an octagonal shape and fits the dimensions of the return flux barrel: the distance between two sides is 3680 mm. The gap between the two weldments is left vacant (except for stiffeners): the outer weldment roles as a clamp for the fringe field which cannot be brought by the inner one.

In downstream direction the diameter of the hole is fixed by the geometrical acceptance of the detector: since the dipole part of the detector is intended to cover an angle of  $10^\circ$  around the beam axis, an opening of 600 mm is needed to let particles exiting at small angles get out of the flux return. The distance between two far sides of the octagon is 4480 mm. The gap between the two weldments hosts a single-layer of muon chambers and a double-layer is foreseen just out of the outer weldment.

### **End Door Skids.**

Each end door is mounted on a skid that is equipped with four 70 t capacity rollers, and four 45 t hydraulic jacks, one in each corner, which allow each of the doors to be moved relative to the barrel for maintenance access. The rollers ride on hardened steel tracks that are permanently located in the floor of PANDA hall. Because the bases of the end doors are narrow compared to their high centers of gravity, 30 t of existing scrap steel is bolted to each skid to lower the center of gravity and move it toward the middle of the skid.

The end doors are bolted either to the barrel of the flux return when in the operating position or to seismic restraint brackets when in the parked position. While the doors are being moved, the 30 t counter weight provides lateral stability for a horizontal acceleration of 0.3 g.

## 6.4 Options and Detailed Design Issues.

A detailed stress and deflection analysis is proceeding for the finalized overall envelope dimensions. A detailed magnetic field and force analysis of the end doors ensures that they will have adequate strength and stiffness to meet all the requirements imposed on them. The tolerance on plate flatness must be defined together with the envelope dimensions of the Muon Chambers. Standard mill tolerances for plate flatness do not meet our requirements for the end door plates to permit reliable MC installation; these tolerances exceed 15 mm, half the nominal gap width. This issue, together with weld distortion in the plates during fabrication, must be resolved with both the plate supplier and the barrel and end door fabricator. Other manufacturing tolerances must be established as the system interface dimensions are finalized.

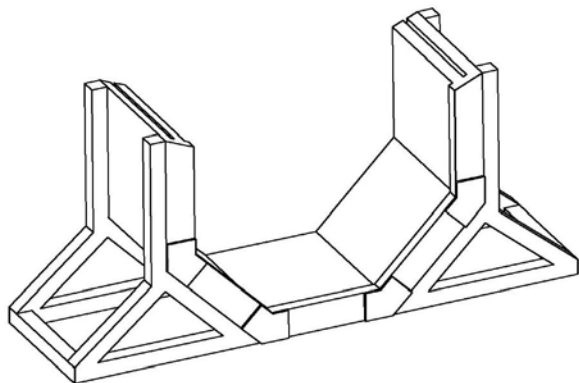


**Figure 17:** Step 1 - Outer base plates placement on back support structure

## 6.5 Procurement, Fabrication, Assembly, and Schedule.

The barrel and the end doors will be built by the same fabricator as part of the same procurement contract. This will eliminate some duplication in the review of vendor qualifications, quality control plans and actions, and many

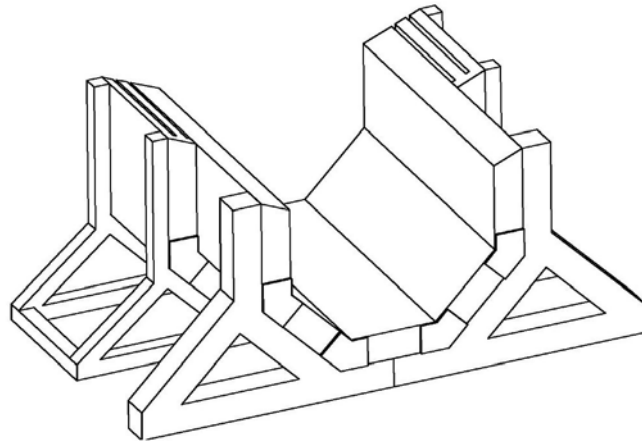


**Figure 18:** Step 2 - Inner lateral plates placement on support structure

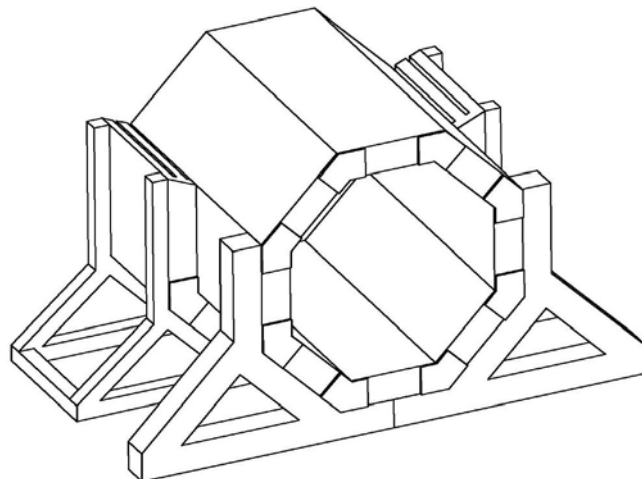


**Figure 19:** Step 3 - Inner top plates placement on lateral plates (an internal support stand is recommended)

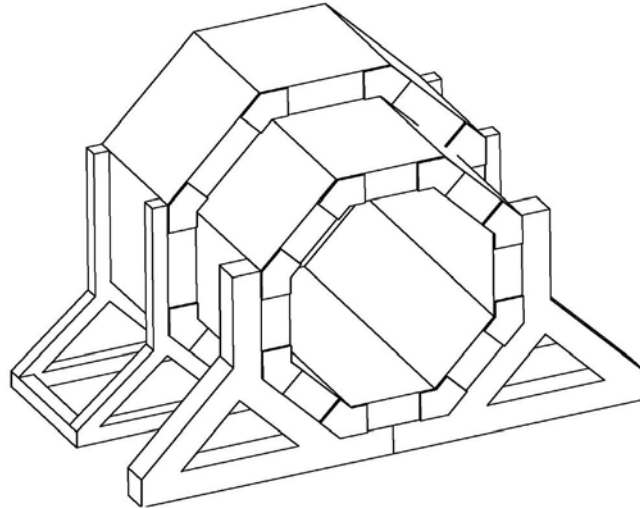


**Figure 20:** Step 4 - Outer top plates placement on inner top plates

contract administration issues. In addition, control of other characteristics of the plate material, such as the chemistry of the plates as it affects weldability and machinability, the mechanical properties of the plate, etc., may be more easily tracked by having one set of acceptance inspection criteria from one supplier for all plates.

The barrel and end doors will be fully assembled and inspected at the fabricator's shop. In this way, any problems that arise can be solved before final assembly in the PANDA hall. This will also permit a thorough review of the assembly procedure by an experienced fabricator and ensure that the necessary lifting and assembly fixtures are functional and are provided with the barrel and end doors. The details of the fabrication and assembly plan will be developed by the fabricator subject to the review of the responsible design engineer in the PANDA collaboration. A proposal for the assembly sequence is provided in Figures 17 to 20.

## **6.6 Compliance with Geometrical Constraints.**

All this project has been realized following the requirements coming from the detectors groups and the integration group. The main requirements can be summarized as follow:

- minimum inner radius of the cryostat: 950 mm (to host all the “barrel” detectors);
- minimum distance between cryostat and upward door: 100 mm (for cabling and services);
- minimum radial distance between cryostat and return yoke: 100 mm (for muon chambers);
- minimum distance between cryostat and downward door: 475 mm (for disc DIRC, downward EMC, cabling and services);
- maximum length of the yoke in upward direction: 1450 mm (to minimize barrel DIRC slabs length);
- maximum length of the yoke in downward direction: 2905 mm (to avoid conflicts with the dipole).

The simultaneous fulfillment of all these requirements and all the magnetic ones made the net axial force arise. We think there is no way to avoid this force without neglecting some of these requirements.

Some preliminary technical drawings are reported in appendix.

## References

- [1] H. Desportes et al., “Construction and Test of the CELLO Thin-Wall Solenoid,” **Ad. Cryogenics Eng.** **25**, 175 (1980).
- [2] ASME, “1992 ASME Boiler and Pressure Vessel Code” (1992).
- [3] EuroCode3, “Design of steel structures”, **EN-1993**.
- [4] CNR, “Costruzioni di acciaio. Istruzioni per il calcolo, l’esecuzione, il collaudo e la manutenzione”, **CNR 10011/97** (1997).
- [5] ANSYS INC, “General Finite Element Code,” Rev. 10.0 (2005).
- [6] M.S. Lubell, “Empirical scaling formulas for critical current and critical field for commercial NbTi”, **IEEE Trans on Mag MAG-19**, 720 (1983).
- [7] D. Andrews et al., “A Superconducting Solenoid for Colliding Beam Experiments,” **Ad. Cryogenic Eng.** **27** (1982).

- [8] E. Baynham and P. Fabbriatore, “Superconducting Solenoid for the BABAR Detector,” **BABAR TDR**.
- [9] A. Bonito Oliva et al., “ZEUS Magnets Construction Status Report,” 11th Int. Conference on Magnet Technology, **MT–11**, 229 (1989).
- [10] P. Clee et al., “Towards the Realization of Two 1.2 T Superconducting Solenoids for Particle Physics Experiments,” 11th Int. Conference on Magnet Technology **MT–11**, 206 (1989).
- [11] H. Desportes et al., “General Design and Conductor Study for the ALEPH Superconducting Solenoid,” **J. Phys. (Paris) C1–341**, (1984).
- [12] Y. Doi et al., “A 3T Superconducting Magnet for the AMY Detector,” **Nucl. Instr. Methods A274**, 95 (1989).
- [13] M.A. Green et al., “A Large Superconducting Thin Solenoid for the STAR Experiment at RHIC,” **IEEE Trans. App. Superconductivity**, 104 (1993).
- [14] C.M. Monroe et al., “The CLEO–II Magnet–Design, Manufacture, and Tests,” **ICEC–12**, 773 (1988).
- [15] M. Wake et al., “Excitation of a Superconducting Large Thin Solenoid Magnet,” **MAG–23**, 1236 (1987).
- [16] F. Wittgenstein et al., “Construction of the L3 Magnet,” 11th International Conference on Magnet Technology, **MT–11**, 131, (1989).
- [17] A. Yamamoto et al., “Thin Superconducting Solenoid Wound with the Internal Winding Method for Colliding Beam Experiments,” **J. Phys. (Paris) C1–337**, (1984).

# Mechanical and Thermal Design of the PANDA Superconducting Solenoid Coil

Andrea Pastorino

Istituto Nazionale di Fisica Nucleare, Sezione di Genova

Via Dodecaneso 33, 16146 - Genova ITALY

March 8, 2007

## Abstract

The subject of this paper is a detailed description of the calculations made during the design process of the INFN Genova concept of the PANDA superconducting solenoid magnet, together with all its essential subsystem and auxiliary structures. Above all, the paper provides evidence of the design choices w.r.t. the results of the mechanical and thermal analyses, and proves the compliance of the Genova concept with PANDA project specifications and international standards.

## 1 Introduction

The design of the PANDA Superconducting Solenoid Thin Coil reported in this phase aims to provide topics for technical evaluations, and general guidelines for the manufacturers. For these reasons, the design does not cover construction details.

First, a complete description of the system is reported, including main functionment processes and geometry, with an important remark: all dimensions provided are at low temperature (i.e.  $\sim 4$  K).

After this, all relevant load scenarios are examined, focusing on the main design aspects and problems; these problems are then investigated by means of preliminary and Finite Element Method calculations.

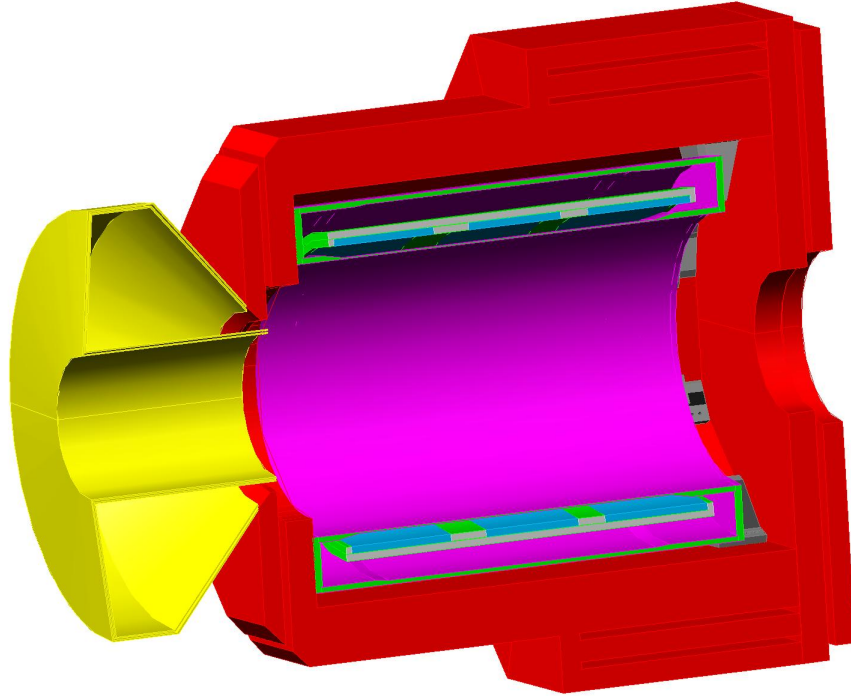


**Figure 1:** The magnet and yoke layout.

Finally, a conclusion chapter discusses results and provides evidence of design choices in terms of reliability, state-of-the-art technology and compliance to international standards.

## 2 System overview

The mechanical and thermal design of the superconducting coil for the PANDA experiment is conservative and within the state of the art for detector magnets. It is based on the experience gained over the past 25 years with thin superconducting solenoids. Although specifically tailored to meet the requirements of PANDA, as well as international standards of quality, the magnet design solutions are similar to many operating detector magnets and therefore very reliable.

The solenoid superconducting coil is constituted of a Rutherford cable, co-extruded with an aluminum stabilizer that allows for adequate quench protection, internally wound into an aluminium alloy coil former. Internally

wounded coils were introduced at the beginning of the 80's, when designers had to face the problem of a detachment of the mandrel and the cable windings in externally wound coils, operating at very low temperature, due to the contraction rates of the different materials and the magnetic pressure. This technique avoids the detachment of the mandrel and the windings, whereas the cable is indeed compressed against the coil former in a more stable configuration.

The aluminium-stabilized Rutherford cable is vacuum-impregnated using an epoxy resin, filled with glass fiber, in order to provide good electrical insulation and mechanical stability. This solution has been preferred, for example to using a pre-preg tape, because it offers a better homogeneity and a higher strength against mechanical stress.

<b>Solenoid Magnet main parameters</b>	
Central induction	2 T
Uniformity in outer tracker	$\pm 2\%$
Coil Former length	$\sim 2.8$ m
Coil former outer radius	1145 mm
Cryostat length	$\sim 3.0$ m
Cryostat outer radius	1350 mm

**Table 1:** Main dimensions and magnetic performance for the PANDA solenoid.

From the thermal point of view, the solenoid coil is indirectly cooled by liquid Helium pipes, connected to the external surface of the coil former. This technique was first developed for CELLO, the first thin solenoid, and has been improved in subsequent designs. The circulation of lHe is either forced or natural, depending on the Helium supply source. The indirect cooling provides a reliable and stable cryogenic system. Table 1 shows the main features of PANDA solenoid design.

## 2.1 Aluminium stabilized Rutherford cable

A Rutherford cable of Niobium-Titanium multifilamentary superconducting strands was clad with pure aluminum using the continuous co-extrusion technique. This cable typology has been widely used in superconducting thin solenoids since the 80's (CDF, BaBar, CMS, ATLAS), with excellent results in terms of stability, quench protection and mechanical performance.

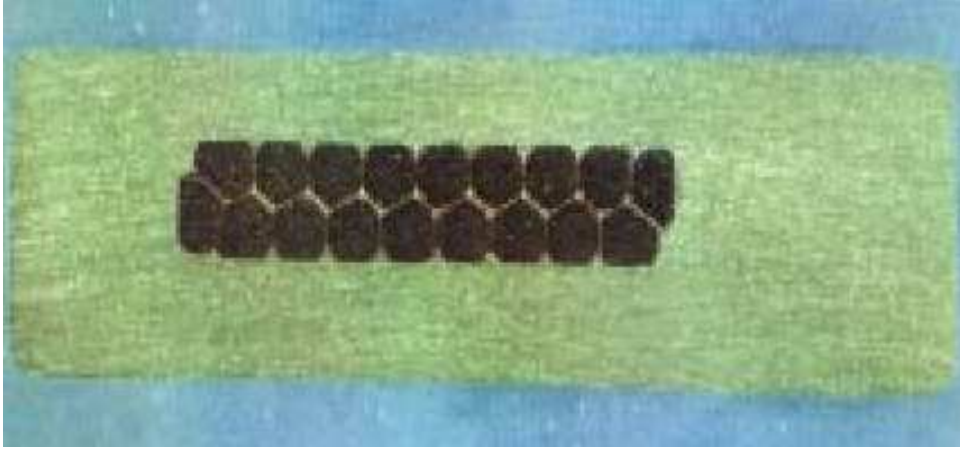


**Figure 2:** Sample Rutherford cable stabilized by Pure Aluminium.

The cable is internally wound into a coil former and is divided in three different windings, each one composed of two layers of cable. In order to have a field homogeneity of  $\pm 2$  T in the large volume specified by the PANDA experiment, the current density in the windings is graded: lower in the central winding and higher in the side ones. The gradation is obtained by using different width conductors: 5.15 mm for the central region and 3.3 mm for the ends. Both conductors are 24.6 mm thick. The different windings are connected through 5 welded cable joints.

The co-extrusion technique ensures a good bonding between Rutherford cable and Pure Aluminium. From the mechanical point of view, the cable is considered homogeneous, taking pure aluminum material properties as a reference for the calculations. Pure Aluminium is a very ductile metal; the transition between elastic and plastic behaviour occurs at  $\sim 20$  MPa in uniaxial tensile strength tests (see Annex A).

## 2.2 Epoxy resin impregnation

Once the winding procedure is terminated, the coil is vacuum-impregnated with a glass-filled epoxy resin, which forms a thin layer between each cable turn, and between the windings and the coil former; the final thickness of this layer is 0.4 mm. The epoxy resin impregnation has different purposes:

- From the electrical point of view, the epoxy layers act as insulators and minimize current diffusion to the coil former, as epoxy has very low electrical conductivity compared to metals.

- As epoxy fills all interstitial gaps between cable wounds, the coil windings are bonded to the coil former and the solenoid magnet is considered as a continuous solid; moreover, epoxy offers a good mechanical strength, especially if compared to Pure Aluminum.
- In case of quench, the thermal conductivity of the impregnation ensures a quick enough propagation and thermal diffusion;

In particular, the glass filled epoxy resin provides a good shear strength and reliability of the bondage in all load conditions (see Annex A).

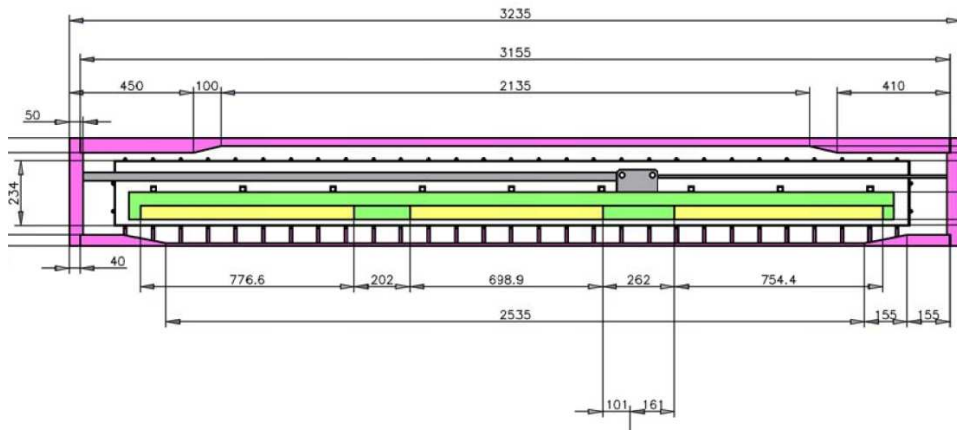


**Figure 3:** Cryostat and magnet layout with quotation.

## 2.3 Coil former

As already mentioned, the solenoid is internally wound into a metallic mandrel; this coil former is composed of a 50 mm thick hot-rolled 5083 T0 aluminium alloy cylindrical shell, with two end rings of the same material (see Annex A for material properties). The purpose of this shell is to provide support for the superconducting cable, housing the three separate windings, as well as limiting deformations under load conditions. In case of quench, and during the cooldown, the coil former ensures a homogeneous and efficient heat distribution along the whole magnet length. The coil former shows two coaxial opposite holes, on the top and the bottom, providing room to the jet or pellet target beam pipes.

Attached onto the outer surface of the coil former are the liquid Helium cooling pipes. These are 9 rings of 5083 T0 Aluminum Alloy, 20 mm in diameter and 2 mm thick cooling pipes, connected by an inlet and outlet main

pipe. This system provides the indirect cooling for the superconducting cable during cooldown and nominal operations.

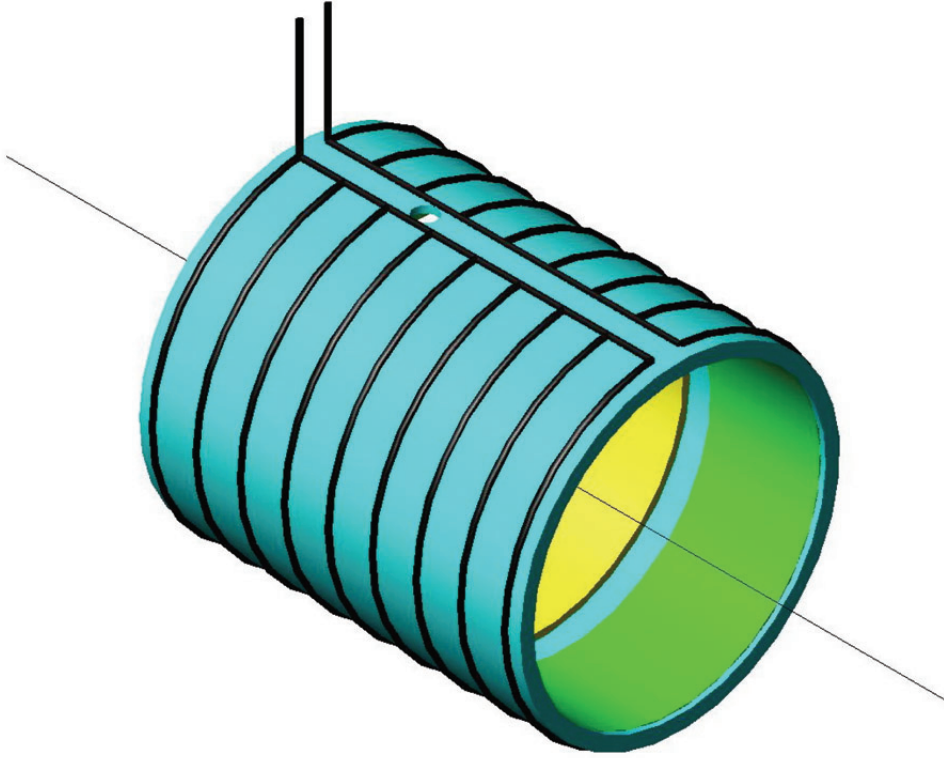


**Figure 4:** Cold mass cooling circuit. The cryogenic supply chimney passes through a cutout in the backward end of the barrel flux return.

## 2.4 Solenoid magnet supports

The PANDA Solenoid Superconducting coil is provided with a complete support system, composed of axial and radial supports. Each single support is a tie rod connected on one side to the external surface of the coil former cylindrical shell, on the other side to the internal surface of the cryostat. The rods are divided into two substantial subgroups:

- the 8 axial tie rods, 30 mm in diameter and  $\sim 1.9$  m long, which take the high axial magnetic forces during nominal operations;
- the 16 radial tie rods, 10 mm in diameter and  $\sim 0.4$  m long, which account for taking the weight of the whole mandrel and solenoid, and

for possible radial forces due to misalignment of the coil;

The complete set of supports is therefore capable to keep the magnet in place during its run, while bearing the magnetic forces.

From a thermal point of view, each rod let a certain amount of heat flux into the magnet, while it is operating at very low temperature. In order to minimize these inleaks while retaining a high material strength, the rods are made of high grade Titanium alloy. Titanium provides a very high tensile strength and a fairly low thermal conductivity, and it has already been used for magnet supports with excellent results (CMS, ATLAS). At the current status of the solenoid magnet design, the choice of the alloy is still open: Titanium grade 5 offers a slightly lower strength but better stability and low fragility at very low temperature if compared to Titanium grade 6 (see Annex A).



**Figure 5:** Titanium alloy raw bars

## 2.5 Cryostat

The Solenoid Superconducting coil and the coil former are enclosed in a cryostat, composed of two coaxial cylindrical shells connected to two annular end flanges. The cryostat ensures that the solenoid operates in vacuum. It is also designed to take the weight of the ECAL, as well as providing docking points for the solenoid supports described in paragraph D. The cryostat gives also room to the Multi-layer insulation (MLI), which minimize heat inleak into the solenoid magnet through radiation. At present, both Aluminium alloy (5083 T0) and Stainless Steel (AISI 304) solutions for the material of the cryostat vessel are taken into account (see Annex A).

Envelope Dimensions	
Inner Radius	950 mm
Outer Radius	1350 mm
Length	~ 3 m
Inner Cylinder Thickness	10 mm
Outer Cylinder Thickness	30 mm
Annular End Plates Thickness	50 mm
Materials	AL5083, AISI 304

Design Loads	
Vessel Weight (steel)	6 t
Cold Mass	5 t
Calorimeter	18 t

**Table 2:** Vacuum vessel parameters.

## 2.6 Cryostat supports

The cryostat provides the insulation and support for the solenoid magnet barrel, together with its cooling system and multi-layer insulation. The barrel, in particular, is suspended on the inner face of the outer sleeve of the vacuum vessel by 16 titanium rods. Besides, the cryostat carries the weight of the Electromagnetic Calorimeter (ECAL), which is attached to the inner sleeve. All these vertical loads (together with the weight of the cryostat itself) shall be transferred to Octagonal Iron Yoke by a suspension system.

Furthermore, the asymmetric shape of the Iron Yoke and the position of the solenoid in the magnetic field generate high axial forces in the supercon-

ducting windings of the solenoid itself. These loads are transferred from the coil barrel to the cryostat by 8 axial titanium rods.

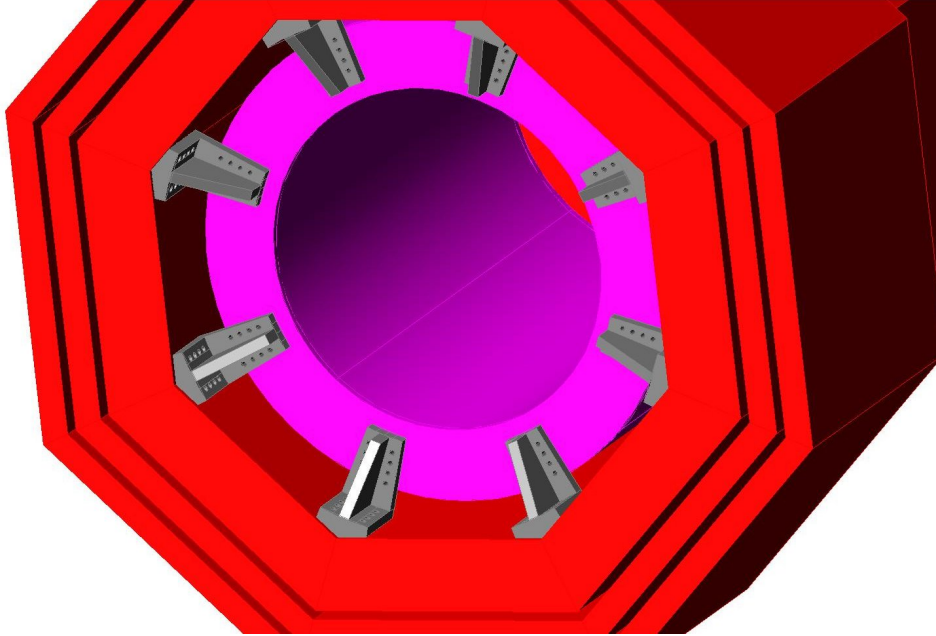


**Figure 6:** Cryostat axial downstream supports in place

In the preliminary concept of the cryostat support system, the high axial forces are taken by eight angular stainless steel supports, placed in the downstream region of the solenoid detector. In the upstream region, eight sliding supports are also placed on the external surface of the vacuum vessel; these, together with the downstream supports, withstand the vertical loads.

The design of the suspension scheme (especially the position of the axial supports) is justified by the following observations:

- The high axial forces are transferred from the solenoid barrel to the downstream flat end of the cryostat by the axial titanium tie rods; with the axial cryostat supports placed in the downstream region, the path of these forces goes directly to the iron yoke, not affecting the inner and outer sleeves and the upward flat end. In this way, any problem of instability due to compression of the vacuum vessel is avoided, since the upstream sliding supports are not capable of taking axial loads.
- With one series of supports at each end of the cryostat, the system is well balanced. With supports only at one side of the cryostat, the

system would have been constrained as a cantilever, increasing loads into the supports and iron yoke.

- Although the presence of the DIRC and the Muon chambers, the downstream region is still the place offering more room for the axial supports. On the upstream side, only 100 mm are left free between the cryostat and the doors, while the space between the cryostat outer shell and the iron yoke is almost as thin. The lack of room could radically compromise the strength and the performance of the supporting structures.
- Supports placed in the central part of the cryostat, between the outer shell and the iron yoke, would be very difficult to access for regulations and maintenance.

## 2.7 Return Yoke

The Return yoke is an octagonal metallic structure enclosing the cryostat; its main purpose is to act as a return path for the magnetic flux, thus insulating external environment from magnetic effects. For this reason, the return yoke is made of ferromagnetic material, structural carbon steel. Moreover, the return yoke provides support for the cryostat and all the main components of the PANDA solenoid magnet. Since many design options are still open for the layout of detectors and equipment within the PANDA solenoid magnet (including a segmented Iron Yoke to host Muon Chambers), the design of the Yoke is still under evaluation.

# 3 Load Scenarios

## 3.1 Nominal Operations

The PANDA Superconducting Solenoid Magnet is supposed to provide an axial magnetic field of 2 Tesla  $\pm$  2% during its normal functioning; to do this, the superconducting Rutherford cable shall operate at very low temperature, around 4.5 K. The windings and Aluminum coil former are kept at this temperature by the liquid Helium cooling system.

The axial and radial components of the magnetic field, generated by the solenoid, give rise to forces in the conductors which are undoubtedly the most relevant mechanical loads on the solenoid magnet. In the axial direction, the forces are unbalanced, because of the asymmetry of the iron yoke and the de-centered position of the coil inside the detector. As calculated by magnetic

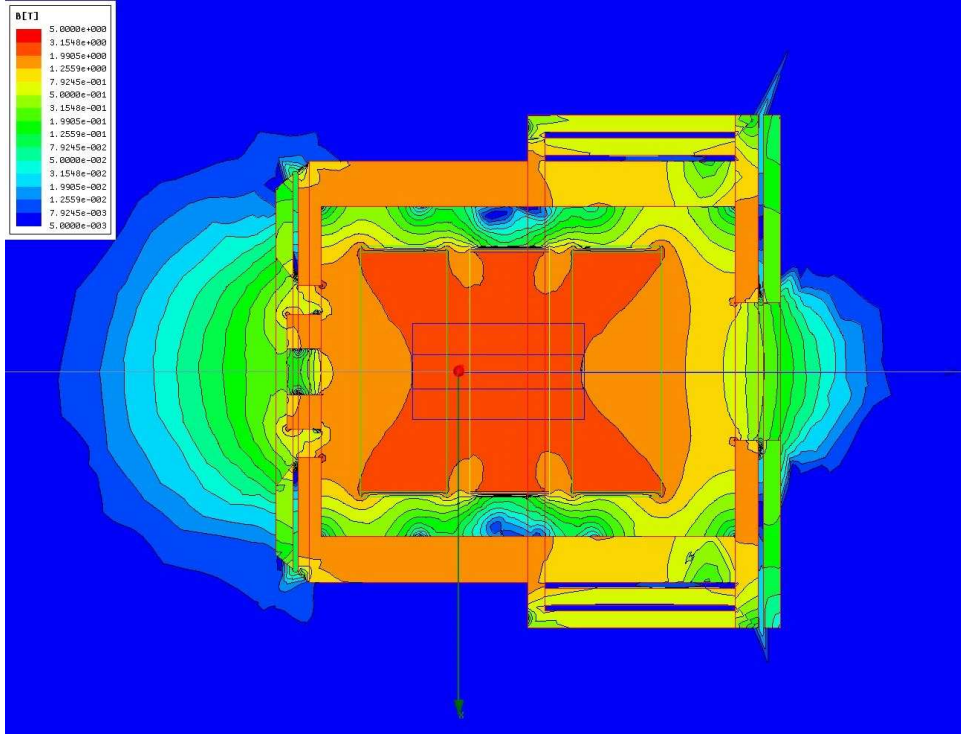


**Figure 7:** Magnetic field distribution over the PANDA detector longitudinal section

analysis software, the resultant axial force is equal to 107 metric tons in the backward direction.

The axial tie rods are loaded with the axial magnetic force, while radial tie rods support the weight of the coil. All these supports are attached to the cryostat, at room temperature (300 K), and temperature decreases along the rods till it reaches 4.5 K in the other end, connected to the coil. In order to minimize heat inleak by conduction through the rod, a 60 K intercept, cooled by liquid Helium, is foreseen in each support.

The cryostat is subjected to the external atmospheric pressure, and bears the weight of ECAL (which is estimated in  $\sim 18$  t) and other equipment (part of the Backward DIRC, most likely the Forward DIRC also). Internally, the cryostat takes the loads coming from the axial and radial tie rods.

Cryostat supports are loaded with forces from the cryostat. These forces are last transferred to the iron yoke.

### 3.2 Nominal Operations with misaligned coil

The position of the solenoid coil inside the iron yoke significantly affects the forces generated in the windings by the magnetic field, forces which rapidly increase or decrease with small displacements. Two different effects are taken into account: a maximum axial positioning error of  $\pm 25$  mm and a maximum radial decentering of 25 mm.

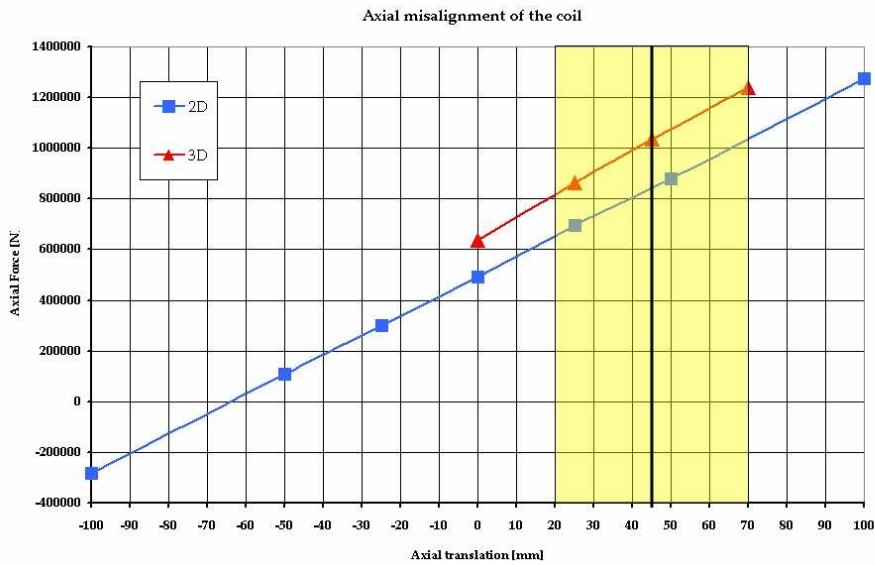


**Figure 8:** Effect of axial misalignment on resultant axial force on the barrel

### 3.3 Cooldown

The solenoid magnet barrel mass, 5.2 t of Aluminum, corresponds to a thermal energy of approximately 850 MJ from 300 K to 60 K, and 20 MJ from 60 K to 4 K. The cooldown of the cold mass will use Helium gas to bring down the temperature from atmospheric values to nominal operations value; the gas flow rate and inlet temperature are gradually diminished in order to limit thermal gradient in the aluminum material up to 40 K.

### 3.4 Warm up

Cold mass warm up, after discharge of the magnet, is achieved by turning off the cooldown circuit, and letting the system temperature increase natu-

rally by heat inleak from the surrounding environment @300 K. No detailed calculations have been made for this load case, since a very slow warm up is expected, the resulting thermal stress in the structures being unharful.

The "Quench" and "Transportation" load cases are still under investigation.

## 4 Calculations

### 4.1 Preliminary Tie Rods Design

The axial tie rods shall be designed in order to withstand the relevant forces generated by the magnetic field in the coil. However, since these supports are also responsible for conduction heat inleak into the solenoid magnet, their dimensions must be optimized.

For symmetry reasons, a number of 8 axial tie rods has been foreseen to withstand the axial magnetic forces. In nominal operating conditions, these rods are assumed to be loaded in pure tension, avoiding any instability issue. The resultant axial magnetic force, as calculated by a magnetic simulation software, is equal to 1.05 MN ( $\sim 107$  t). Hence, the axial load on each rod is

$$N = \frac{1.05 \text{ MN}}{8} = \sim 131 \text{ kN}.$$

The design axial load is the axial load  $N$  multiplied by a factor of 1.15, to take into account of the possible errors in calculating the magnetic forces. Therefore, the design axial load for each rod is

$$N_d = 1.15 \cdot N = \sim 151 \text{ kN}.$$

As pointed out in Annex A, the admissible strength limit for the Titanium tie rods (grade 5) is equal to 275 MPa. The minimum cross section area of a single rod is then calculated from the formula:

$$\sigma_{adm} \geq \frac{N_d}{A}$$

giving  $A \geq 549 \text{ mm}^2$ , or a diameter of at least 26 mm.

The 16 radial tie rods are responsible of taking the weight of the coil during nominal operations, other than preventing possible additional forces due to misalignment. In a conservative assumption, only four rods account for taking the load (pure tension) in the following preliminary calculations. The estimated weight of the coil former + solenoid windings is  $W = 51 \text{ kN}$

( $\sim 5.2$ t), therefore the load applied on each radial tie rod (included the 1.15 multiplying factor) is

$$V = \frac{1.15 \cdot 51 \text{ kN}}{16} = 14.5 \text{ kN}$$

on each radial rod.

As for the axial supports, the minimum cross section area of a single radial support is calculated from:

$$\sigma_{adm} \geq \frac{V}{A}$$

giving  $A \geq 53 \text{ mm}^2$ , or a diameter of at least 8 mm.

The solenoid coil supports are one of the main heat sources in the coil thermal budget. The amount of the heat inleak into the system must be minimized in order to reduce liquid Helium consumption of the refrigerating system.

Heat flows from the external environment (@300 K) to the coil former ( $\sim 4.5$  K) through the tie rods by means of thermal conduction. In a steady state heat transfer regime, the conduction heat flux is calculated as follows:

$$q = \frac{A}{l} \int_{4.5}^{300} k(T) dT$$

where  $k$  is the thermal conductivity of the material,  $A$  is the cross section area of the rod and  $l$  is the length. Once the material has been chosen (Titanium), heat flux can be reduced by diminishing the cross section area and increasing the rod length.

Another way to reduce heat inleaks is to introduce a 60 K liquid Helium intercept at the center of the bar length. As a consequence, part of the flux is taken by the intercept, and the heat inleak into the coil is:

$$q = \frac{2A}{l} \int_{4.5}^{60} k(T) dT$$

Hence, the heat inleak for a single axial tie rods is calculated assuming a cross section area equal to  $707 \text{ mm}^2$  (rod diameter 30 mm) and a length of  $\sim 1.9$  m. The calculated heat flux of a single axial rod is 0.13 W. The contribution of the radial tie rods is calculated using the same procedure and assuming a cross section area equal to  $79 \text{ mm}^2$  (rod diameter 10 mm) and a length of  $\sim 0.4$  m. The calculated heat flux of a single radial rod is 0.07 W.

The magnetic calculation of the forces have been iterated with the coils misaligned in several positions, moving the barrel along the axis of symmetry of the magnet, and in the radial direction also. The axial resultant forces

increase by  $\sim 9$  kN each millimeter of displacement in the backward direction. With the forementioned suspension system, the stability is ensured by the stiffness of the 8 axial rods, some 42 kN/mm, more than 5 times greater than the forces increase ratio.

## 4.2 Preliminary Solenoid Coil Heat Budget

The amount of lHe @4.5 K needed for the solenoid magnet refrigeration during nominal operations can be calculated on the basis of a heat inleak budgeting, which accounts for the main different heat sources in contact with the solenoid coils and coil former.

The total heat flow @4.5 K due to the coil supports is calculated multiplying the single heat inleaks for the number of the rods (8 axial and 16 radial).

The radiation heat flow rate coming from the Multi-Layer Insulation (MLI) is assumed to be equal to  $0.07 \text{ W/m}^2$  @4.5 K. Hence, since the total surface of the MLI enclosing the magnet is  $\sim 44 \text{ m}^2$ , the total heat inleak due to radiation is 3.08 W.

A summary of the budget is reported in the table below, including the estimated contributes from the cryo-chimney, gas load and cable joints. Eddy currents heat generation is reported, but this effect occur during magnet charge only. As a result, the maximum heat flow into the solenoid during magnet charge is equal to 28.28 W.

Source	Heat flow
Axial tie rods	1.07 W
Radial tie rods	1.13 W
Radiation	3.08 W
Cable joints	2 W
Cryo-chimney	10 W
Gas load	1 W
Eddy currents	10 W
<b>Maximum heat load (during charge)</b>	<b>28.28 W</b>
<b>Nominal heat load</b>	<b>18.28 W</b>

**Table 3:** Solenoid magnet Heat Budget @4.5 K

This heat load is dissipated by liquid Helium evaporation. As already pointed out, the coil former is refrigerated by a two-phase lHe circuit, fed either by forced or natural convection (thermo-syphon). For this purpose, we

assume that 10% of the liquid Helium mass flow evaporates, with a latent heat ( $\lambda$ ) of 20100 J/kg. A multiplying factor of 2 is applied to the maximum heat load for conservative reasons. Thus the fraction of the mass flow evaporated is:

$$\dot{m}_g = \frac{2 \times \dot{q}}{\lambda} = 2.814 \text{ g/s}$$

and the needed lHe mass flows is 28.14 g/s (ten times  $\dot{m}_g$ ), with a liquid fraction of  $\sim 80 - 85\%$  (as a comparison, BaBar lHe mass flow was  $\sim 25$  g/s, with a cold mass of 4.9 t).

### 4.3 Solenoid Magnet Finite Element Structural Analysis

During nominal operating conditions, the three windings of the superconducting coil generate a magnetic field aiming at reaching an axial component of  $2 \text{ T} \pm 2\%$  along the detector axis. The iron yoke then provides a return path for this flux, thus the solenoid coil is permeated by a complex magnetic field. The forces generated in the conductors of the solenoid (due to Lorentz's law) show very strong axial and radial components. Radial forces are positive (directed outwards with reference to the coil cylinder) and uniform along the winding circumference. Axial forces change their sign going from one end of the solenoid to the other; as a result, the windings are compressed in the axial direction, as magnetic forces push them against the coil former rings which divide the windings themselves. The magnetic calculations report that the total values of these loads are equal to 333 t for the first winding,  $-4$  t in the second and  $-436$  t in the third. As a result of these magnetic loads, the resultant axial force is directed upstream and equal to  $-107$  t, and the solenoid coil is compressed in the axial direction.

As already mentioned in this report, the coil windings are composed of a pure aluminium (a very ductile metal) stabilized Rutherford cable impregnated by epoxy resin filled with glass fiber (an orthotropic material, acting as a glue between the cable windings). The stability of the magnet assembly under the action of the magnetic forces is investigated through a Finite Element Model. A longitudinal section of the coil barrel is simulated using 2D axisymmetric plane elements which faithfully reproduce the cable sections, the epoxy resin impregnation and the aluminium alloy coil former.

The Rutherford cable is simulated as a uniform pure aluminium section, with a non-linear stress strain curve, in order to take into account material plastic behaviour. A detailed sampling of the magnetic radial and axial fields has been transferred from the magnetic simulation to the FEM structural;

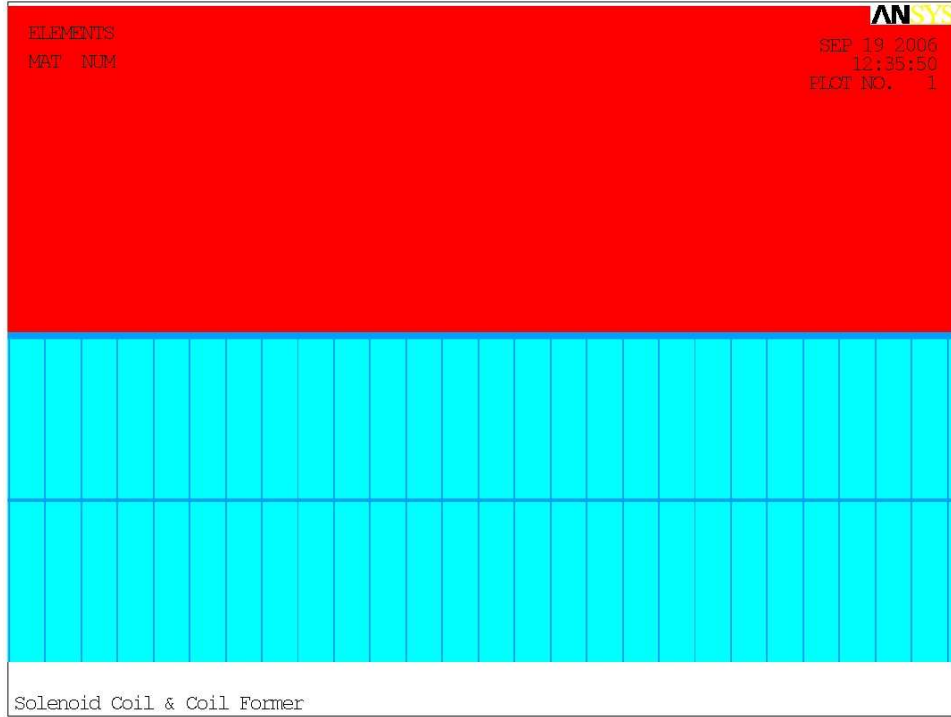


**Figure 9:** Detail of the barrel longitudinal section - Aluminium Coil Former, Epoxy Impregnation and Rutherford Cable Elements.

magnetic forces on the superconducting cable sections are then calculated as follows:

$$F_r = B_z \cdot i \cdot l = B_z \cdot (\rho \cdot A) \cdot (R \cdot d\theta)$$

$$F_z = B_r \cdot i \cdot l = B_r \cdot (\rho \cdot A) \cdot (R \cdot d\theta).$$

Each cable section is composed of two adjacent elements, delimited by six nodes, four of them being corner nodes, and two central nodes. The magnetic forces are calculated in each node, therefore  $R$  is the radius coordinate,  $B$  is the field component in the node,  $\rho$  is the current density of the coil,  $A$  is the area of the cable section assigned to each node, that is  $1/8 \cdot A$  to corner nodes and  $1/4 \cdot A$  to central nodes. Since the model is axisymmetric,  $d\theta$  is integrated along the whole circumference, giving  $2\pi$ . The axial resultant calculated with the above formula is equal to 1.21 MN, with a load magnification factor of 1.15 w.r.t. the nominal value of 1.05 MN.

Structural constraints are placed in nodes on the outer radius of the coil former corresponding to the fixing hinges of the axial support; only the axial

translational degree of freedom is constrained, as the model is axisymmetric.

The result of the finite element simulation is summarized in the following major points:

- global deformations are very limited, thanks to the coil former. Maximum radial expansion is 0.65 mm, whereas axial contraction is up to 0.47 mm;
- stress in the pure aluminium elements exceeds the elastic limit of the material. As a consequence, the superconducting cables work in plastic domain, with an equivalent plastic stress of 33 MPa, corresponding to a plastic strain of 0.22. A further analysis points out that hoop stress (26 MPa) is the most relevant contribute for pure aluminium stress condition, the radial forces pressing the cables against the coil former wall. While the deformations of the cable are completely limited by the coil former, plastic behavior is unlikely to take place after the first magnet charge because of material hardening and repositioning of the cables in space.
- Epoxy resin impregnation maximum equivalent stress is 16 MPa, this value being well within the material capabilities. Furthermore, the maximum shear stress is equal to 3.04 MPa, about 1/10 of epoxy shear limit.
- The coil former is loaded well below its elastic limit, thus containing the deformations of the solenoid coil with no particular effort. The maximum equivalent stress is equal to 46 MPa and the maximum hoop stress is 43 MPa.

#### 4.4 Solenoid Magnet Finite Element Thermal Analysis

The superconducting cable of the PANDA solenoid magnet operates @4.5 K in nominal conditions. The stability of this temperature is essential for maintaining the superconductivity regime into the cables and keeping the value of the critical current above the operating current of the magnet, thus avoiding quench. A finite element steady state thermal model has been built to calculate the temperature distribution into the solenoid magnet during operations. It is a 3D solid model of 1/8 of the solenoid and coil former, together with parts of the refrigeration pipes.

The thermal model is simplified considering the Rutherford cable and the epoxy impregnation as a single material, with equivalent thermal conductivity either in the radial, hoop and longitudinal direction. Heat loads are taken from the preliminary heat calculations: the cryogenic chimney and gas loads

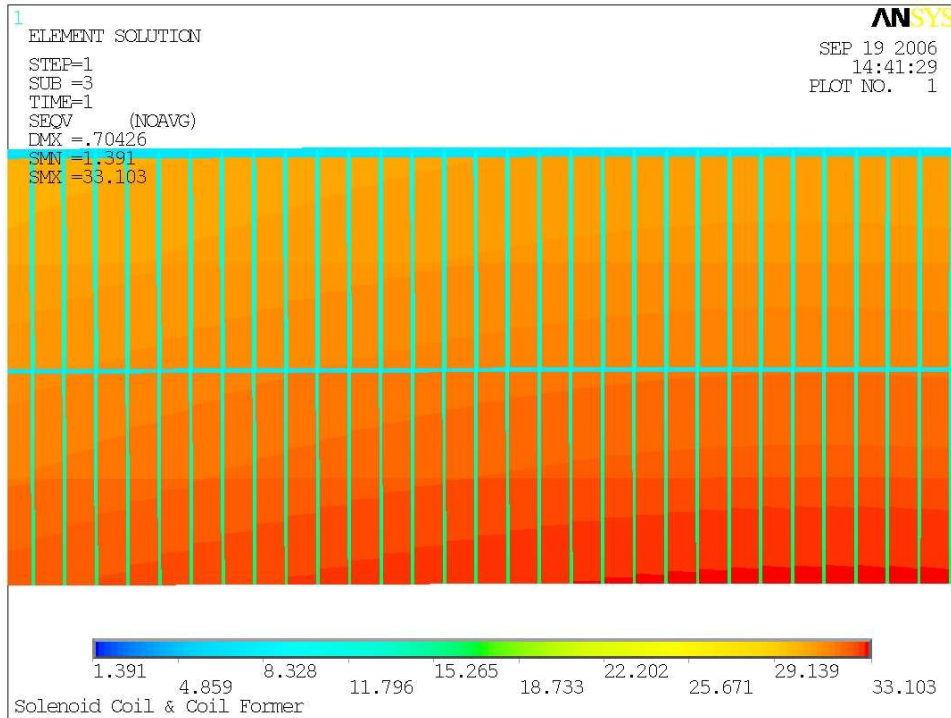


**Figure 10:** Von Mises equivalent stress in Rutherford Cable and Epoxy elements.

are distributed on the external surface of the barrel (as radiation), whereas cable joints heat inleak is spread over the whole cable volume. The heat coming from the supports (1 axial rod and two radial in 1/8 of the solenoid) are concentrated in the zones where the attachments are foreseen. The refrigeration is simulated constraining the temperature of the internal surface of the lHe pipes @4.5 K, assuming therefore a cooling efficiency of 100% (which is, by the way, very close to reality). This non-conservative assumption is balanced applying a magnifying factor of 2 to all heat loads.

The results show a peak temperature of @5.37 K, located at the attachment of a radial support on the coil former, and a maximum  $\Delta T$  of @0.66 K (@5.16 K temperature) in the cable windings. The calculated heat absorption of the refrigeration system is @5 W for 1/8 of barrel, thus @45 W total.

The same analysis, with no magnifying factor applied on the loads, returned a  $\Delta T$  of @0.32 K in the cable and a total heat absorption of 22 W for the refrigerating system.

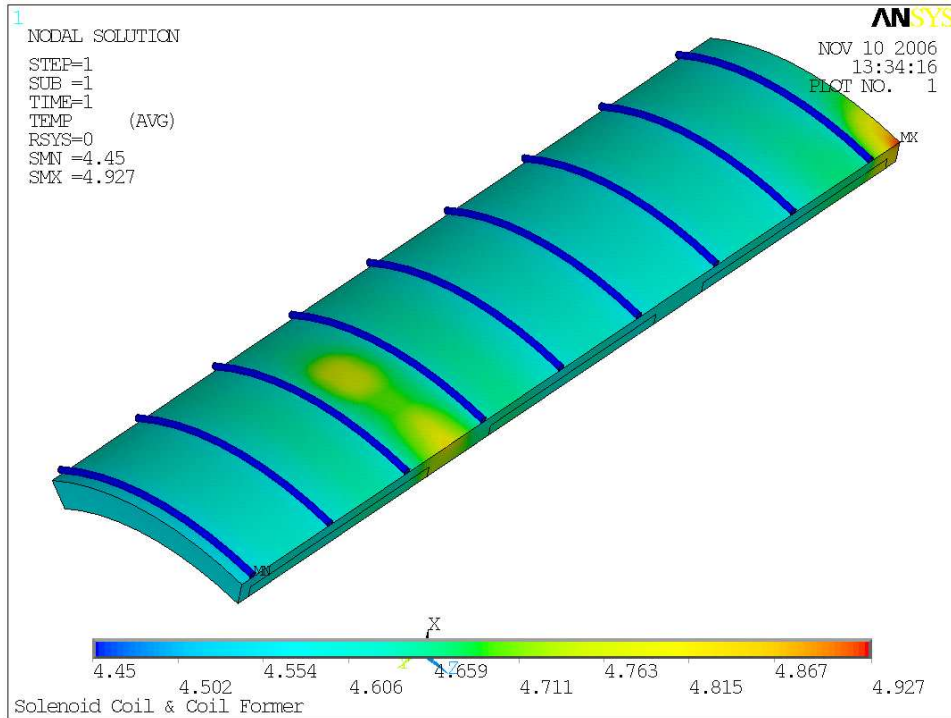


**Figure 11:** Temperature distribution over 1/8 of barrel.

## 4.5 Cryostat Design

The annular vacuum vessel enclosing the solenoid magnet coil is designed according to ASME Code for Pressure Vessels, 8th Edition. The code compliance is actually restricted to the thicknesses of internal and external shells as well as for the flat annular heads (for detailed calculations, see Annex X).

In nominal conditions, the cryostat is loaded with external atmospheric pressure, while vacuum is generated inside the vessel. Additional concentrated loads (magnetic forces transmitted by the Titanium tie rods and weight of the ECAL) are not taken into account in the Code design, but will be included in the FEM model.

The minimum thickness required for the internal shell is 2 mm. The nominal thickness is 10 mm.

The ASME procedure to calculate the minimum thickness of a cylindrical shell under external pressure is iterative. Hence, a tentative value of 15 mm is assumed for the thickness. This assumption fulfills the minimum requirements for maximum pressure allowed. The nominal thickness is equal to 30 mm.

The minimum calculated thickness for the annular flat plates is 10 mm.

The nominal thickness is 30 mm for the forward plate and 60 mm for the backward plate, which bears the solenoid axial supports.

The response of the Vacuum Vessel to the concentrated loads is investigated by a structural static finite element analysis. Besides the uniform atmospheric pressure distributed on the external surface of the annular vessel, the loads transmitted by the axial tie rods, and the weight of the ECAL equipment are included.

The total axial magnetic resultant of 107 t is multiplied by a magnifying factor of 1.15 and applied on the backward flat plate, split among the 8 zones where the rods are attached.

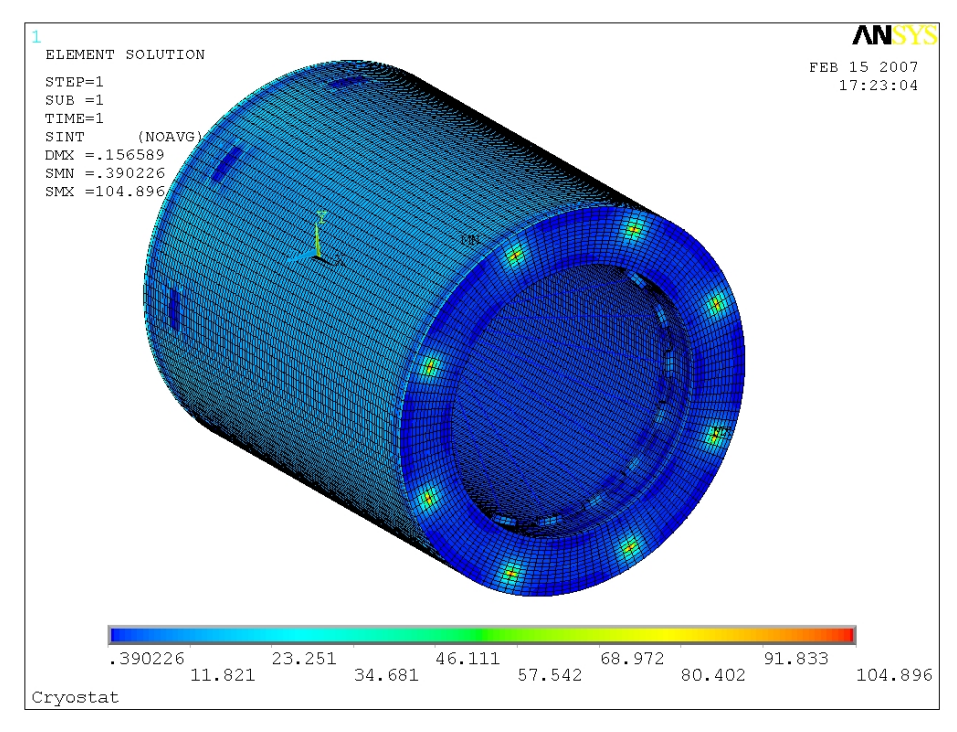


**Figure 12:** Equivalent stress in Vacuum Vessel (AISI 316)

The ECAL barrel is attached to the inner sleeve of the cryostat. At present, two reinforced rings are foreseen, which support the ECAL by means of 2 x 16 lugs, each one provided with a bolted connection. In order to simulate the weight of the equipment (180 kN multiplied by 1.15), the force is applied in the center of gravity of the ECAL and then transmitted to the 32 lugs by infinitely rigid elements (MPC).

The cryostat is constrained by two different orders of supports. On one

side, 8 bolted plates, strengthened with ribs, are attached to the backward flat head of the vessel. The purpose of these structures is to take the axial loads of the internal tie rods and transfer them directly to the Iron Yoke. The weight of the cryostat and ECAL equipment is then shared between these structures and 8 sliding supports, located on the external surface of the vessel, near the forward end. These supports are designed to take only vertical loads, in such a way that the cryostat is not compressed by the axial magnetic forces transferred by the internal supports.

All the shells, plates and rings of the Vacuum Vessel are made of the same material. Two distinct calculations are made, the first using 5083-T0 Aluminium Alloy, and then AISI 316 Stainless Steel.

The results show the cryostat is able to withstand all the mentioned loads. The maximum calculated stress in the Aluminium Alloy design is equal to 97 MPa, and 104 MPa for Stainless Steel. This peak is located at the connections between the forward plate and the solenoid axial supports, where the 107 t axial forces are applied.

## 4.6 Cryostat Supports Design and FEM Analysis

At the present status of the design process, the 8 cryostat axial downstream supports are constituted of two welded plates, joined together forming a 90 degrees corner, reinforced by a thick transversal triangular plate. These supports are bolted to the downstream flat end of the cryostat, and to the iron yoke. Infact the axial downstream supports also act as a hinge between two different octal bars of the iron yoke, fixing them together in the downstream end.

The eight axial downstream supports are designed to withstand the 107 t axial magnetic force, multiplied by a factor of 1.15, to take into account of uncertainty in calculations or coil misalignment. The thickness of the three different plates composing the supports is set to 60 mm. The cryostat is suspended to each support by means of  $8 \times M30$  bolts UNI-ISO 4536 Class 8.8. Another 8 bolts fix each support to the iron yoke. An M30 Class 8.8 alone is capable to withstand a maximum axial force equal to  $\sim 36$  t. Manual calculations and simulations show that the maximum axial load on a single bolt does not exceed 4.6 t, both on the cryostat side and the iron side. Hence, eight bolts on each side are capable to withstand the loads in nominal conditions without any problem.

The strength of the support structure was analysed by a finite element model of the 3D solid under nominal conditions. The solid model was meshed with second-order tetrahedral elements, and stainless steel material properties were included. The axial and vertical loads were applied at bolts locations

on the cryostat side, and the model was constrained on the iron yoke side. As a result, the axial support appears to be strong enough to withstand all loads in nominal conditions. The maximum stress is equal to  $\sim 113$  MPa, where the elastic limit for AISI 316 Stainless Steel is 205 MPa. Nevertheless, the stress peaks (concentrated on the edges of the bolt holes) are due to geometrical issues of the solid model; the actual maximum stress reach up to  $\sim 60$  MPa, thus offering an even higher margin of safety.

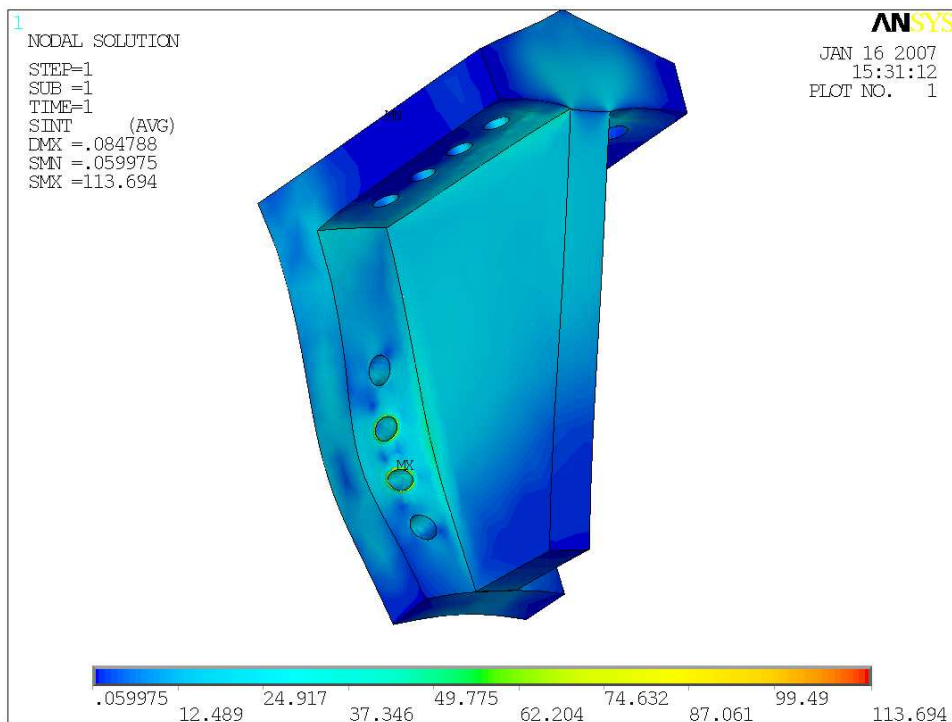


**Figure 13:** Axial Downstream Support Maximum Stress

The design of the upward vertical cryostat supports is still under development; nevertheless, they are characterized by fairly low vertical loads, but they need to provide the axial degree of freedom for the cryostat.

#### 4.7 Cooldown Time and Helium Requirements

The cooldown of PANDA Solenoid Magnet will be made by letting Cold Helium Gas into the cryogenic refrigeration system; the temperature of the gas will be monitored to prevent high thermal gradients in the system. Assuming a maximum thermal gradient of 40 K in the magnet barrel, and a constant

Helium gas flow of 50 g/s at 1.25 bar and decreasing temperature, the cooling gas is capable to absorb a heat flux ranging from  $\sim 7$  kW @ 260 K to  $\sim 4$  kW @ 4 K. Taking into account the heat inlets from solenoid supports and thermal shields, these assumptions lead to a cooldown time of at least 1.5 days, but most likely 2.5 days including also cooldown of the shields and supports.

## 4.8 Thermal Contractions

The effect of thermal contractions cannot be underestimated in the design of the PANDA Solenoid Magnet. The components of the assembly are made of different materials, which in some cases have quite different reactions to very low temperature. While it is clear that almost all technical materials contract at cryogenic temperatures, the effect of different contraction ratios on the structural behavior of a complex structured can have dramatic consequences. The PANDA Solenoid Barrel, in Genova group concept, is a quite homogeneous Aluminium item, the Epoxy impregnation and superconducting cable strands being a minor percentage, distributed evenly along the barrel. For this reason, the main concern is to give the barrel the freedom to contract, while still being attached to the axial and radial supports. This effect is achieved mainly by releasing the axial degree of freedom for the radial supports. As a result, the barrel is able to contract along the axis, and as a secondary effect is translated in the forward direction by the contraction of the axial rods. The effect of the radial contraction of the barrel on the support system is expected to be negligible.

## 5 Conclusions

During Nominal Operation the mechanical and thermal performance of the PANDA Solenoid Magnet is stable.

The axial compression and radial pressure in the coil windings, generated by the magnetic field, are well contained by the Aluminum Coil Former, while the Epoxy Impregnation guarantees the bonding of the barrel without exceeding its strength capabilities, especially about shear stress.

The high axial resultant force on the barrel, due to the asymmetrical layout of the Magnet and Iron Yoke, is taken by the Titanium Axial Rods with a significant margin of safety. The same result is achieved by the Titanium Radial Supports, to which the Barrel is suspended. The stability of the equilibrium of the magnet in its nominal position is guaranteed by the high axial stiffness of the rods.

The Cryostat Vacuum Vessel is designed according to international standards (ASME Code), under the action of the external pressure. The Vessel is also capable of withstanding all the additional concentrated loads, due to the internal Solenoid Barrel supports, the weight of the electromagnetic calorimeter and other equipment. The current concept for the Suspension System of the Cryostat offers good stability and strength against all loads transferred to the Iron Yoke. A final decision on this supports will occur as soon as the internal layout of the detector is freezed.

A mechanical analysis of the PANDA Iron Yoke has not yet been performed, again because the internal layout of the detector is still under development, this matter being of great influence on how the loads are transferred to the Yoke. Nevertheless, questions are still pending wether the Yoke Barrel should be segmented or not, to house Muon Chambers. This would also dramatically affect the way the loads are transferred to the Yoke.

From the thermal point of view, the PANDA Solenoid Magnet Cooling System relies on solid experience from past thin solenoid detectors. The calculated heat budget and cooling system requirements are reasonable if compared with similar existing experiments (BaBar), while fulfilling its purpose.

## 6 References

R.P. Smith et al., "The Aluminum Stabilized Conductor for the Fermilab D0 Solenoid", 16th International Cryogenic Engineering Conference, Kitakyushu, Japan, May 20-24, 1996

R.A Bell et al., "The BaBar Superconducting Coil: Design, Construction and Testing", 15th International Conference on Magnet Technology, Beijing, China, October 22-24 1997

"Safety Assessment Document - BaBar", Stanford Linear Acceleration Center - Research Division

B. Blau et al., "The CMS Conductor", Dapnia, CEA, Saclay, France, September 24 2001

F. Rondeaux et al., "Thermal Conductivity Measurements Of Epoxy Systems At Low Temperature", Cryogenic Engineering Conference Madison, WI, USA, July 20-21 2001

B. Lavery et al., "Design and Test of the Titanium Alloy Tie Rods for the CMS Coil Suspension System", Dapnia, CEA, Saclay, France, September 24 2001

M. Reytier et al., "Characterization Of Titanium Alloys For Cryogenic Applications", CEA, Saclay, France

F. Kircher et al., "CMS Coil Design and Assembly", Dapnia, CEA, Saclay, France, September 24 2001

BaBar Collaboration, "BaBar Technical Design Report", SLAC, March 1995

R. Fast et al., "Design Report for an Indirectly Cooled 3-m Diameter Superconducting Solenoid for the Fermilab Collider Detector Facility", Fermilab, October 1 1982

# AnneX A - Material Properties

Since strength properties increase with decreasing temperature for all the materials listed in this Annex, as a conservative assumption all strength properties are reported @ room temperature (300 K).

## I. PURE ALUMINUM (RRR 1200)

Mass Density	2650	kg/m <sup>3</sup>
Elastic Strength	20	MPa
Ultimate Strength	47	MPa
Young's Modulus	67000	MPa
Poisson's Ratio	0.33	
Thermal Contraction Ratio (@4 K)	4.2	mm/m

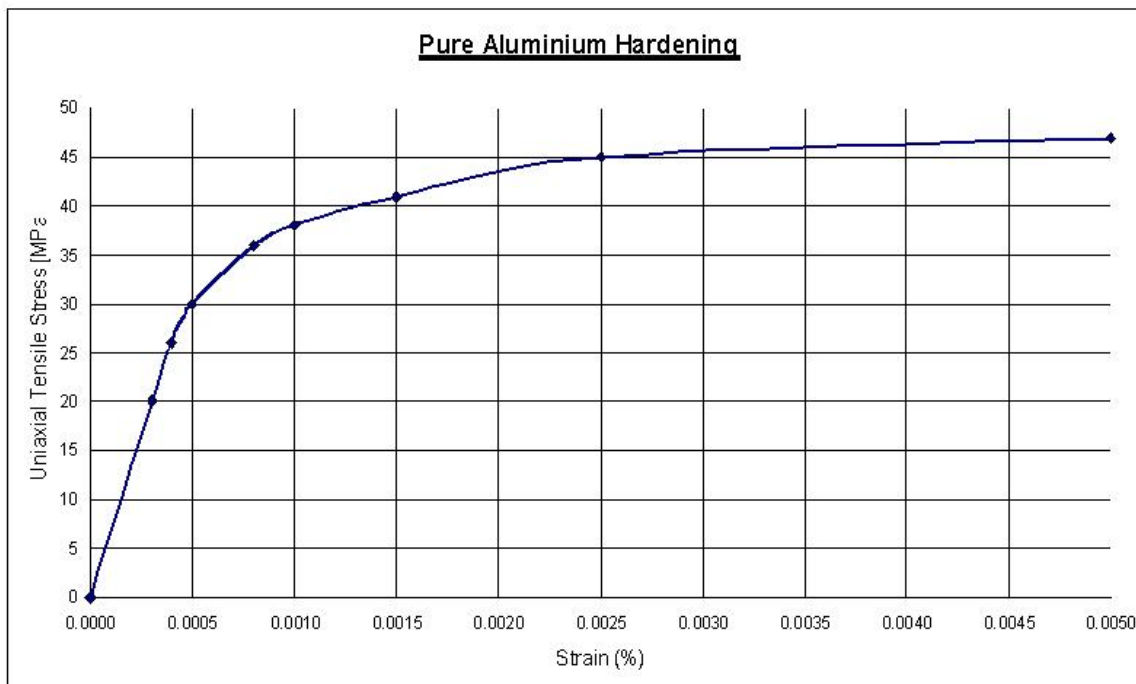


**Fig. 1:** Pure Aluminum Stress-Strain Curve.



**Fig. 2:** Aluminum Specific Heat.

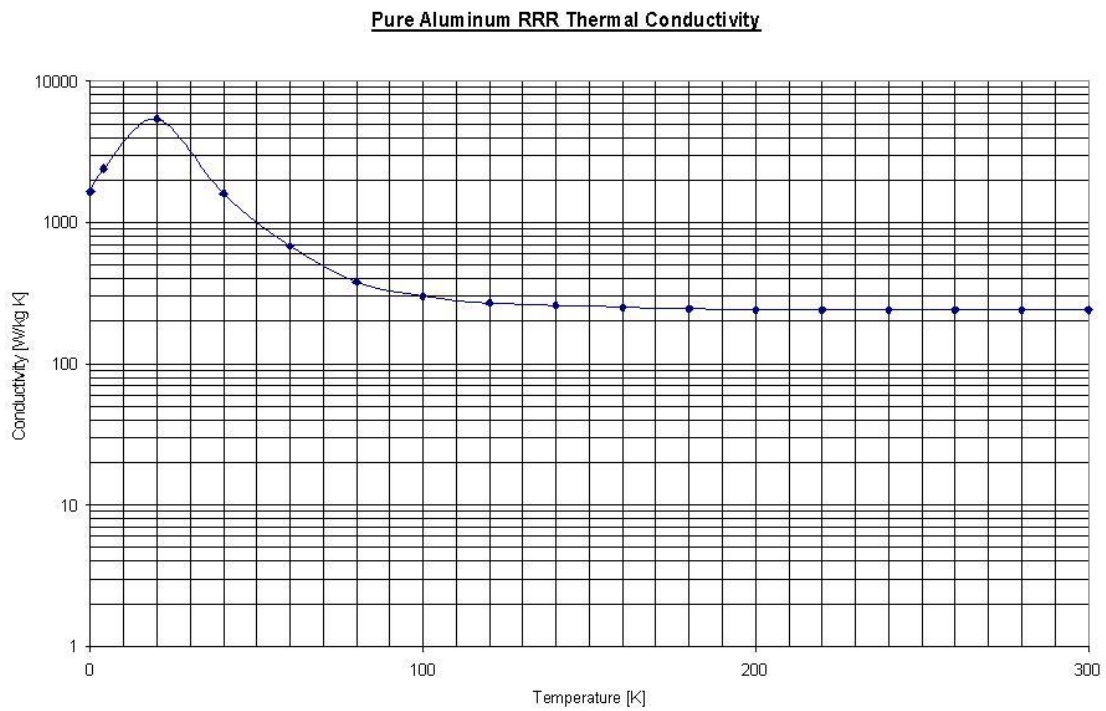


**Fig. 3:** Pure Aluminum Thermal Conductivity.

## II. 5083 T0 ALUMINUM ALLOY

Mass Density	2660	kg/m <sup>3</sup>
Elastic Strength	145	MPa
Ultimate Strength	300	MPa
Allowable Elastic Stress	72	MPa
Allowable Ultimate Stress	100	MPa
Young's Modulus	71000	MPa
Poisson's Ratio	0.33	
Thermal Contraction Ratio (@4 K)	4.2	mm/m

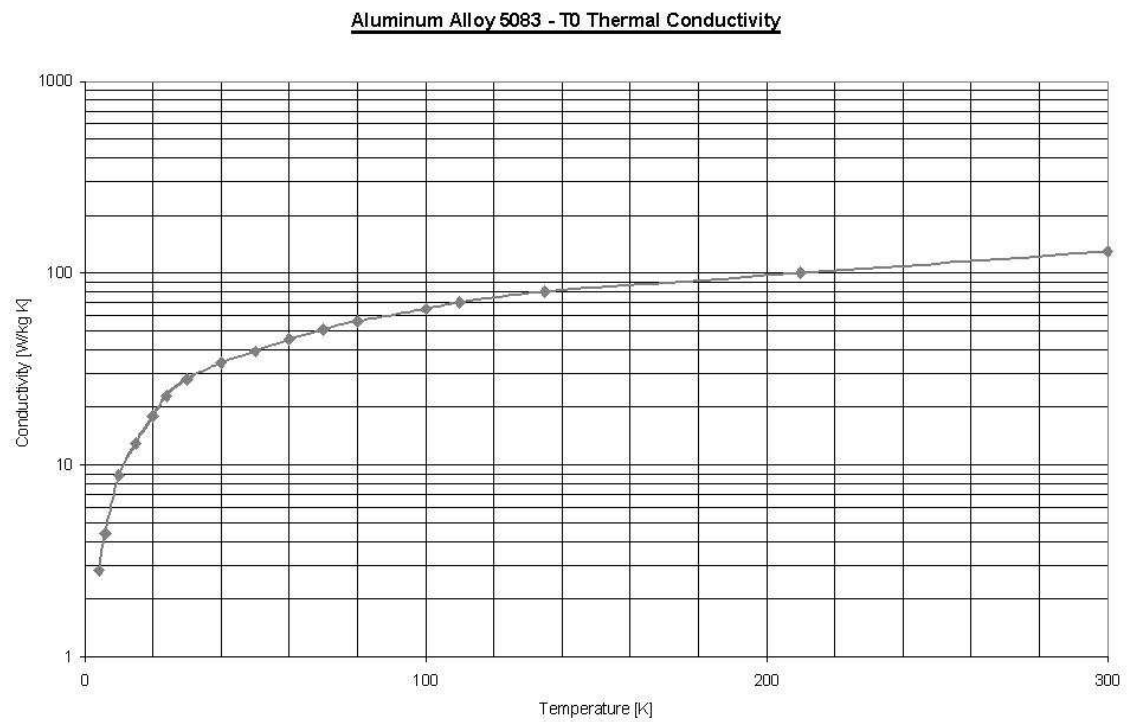


**Fig. 4:** 5083 T0 Aluminum Alloy Thermal Conductivity.

### III. AISI 304L STAINLESS STEEL

Mass Density	8050	kg/m <sup>3</sup>
Elastic Strength	205	MPa
Ultimate Strength	510	MPa
Allowable Elastic Stress	102	MPa
Allowable Ultimate Stress	170	MPa
Young's Modulus	198000	MPa
Poisson's Ratio	0.3	
Thermal Contraction Ratio (@4 K)	3.0	mm/m

### IV. AISI 316 STAINLESS STEEL

Mass Density	8050	kg/m <sup>3</sup>
Elastic Strength	250	MPa
Ultimate Strength	565	MPa
Allowable Elastic Stress	125	MPa
Allowable Ultimate Stress	188	MPa
Young's Modulus	193000	MPa
Poisson's Ratio	0.3	
Thermal Contraction Ratio (@4 K)	3.0	mm/m

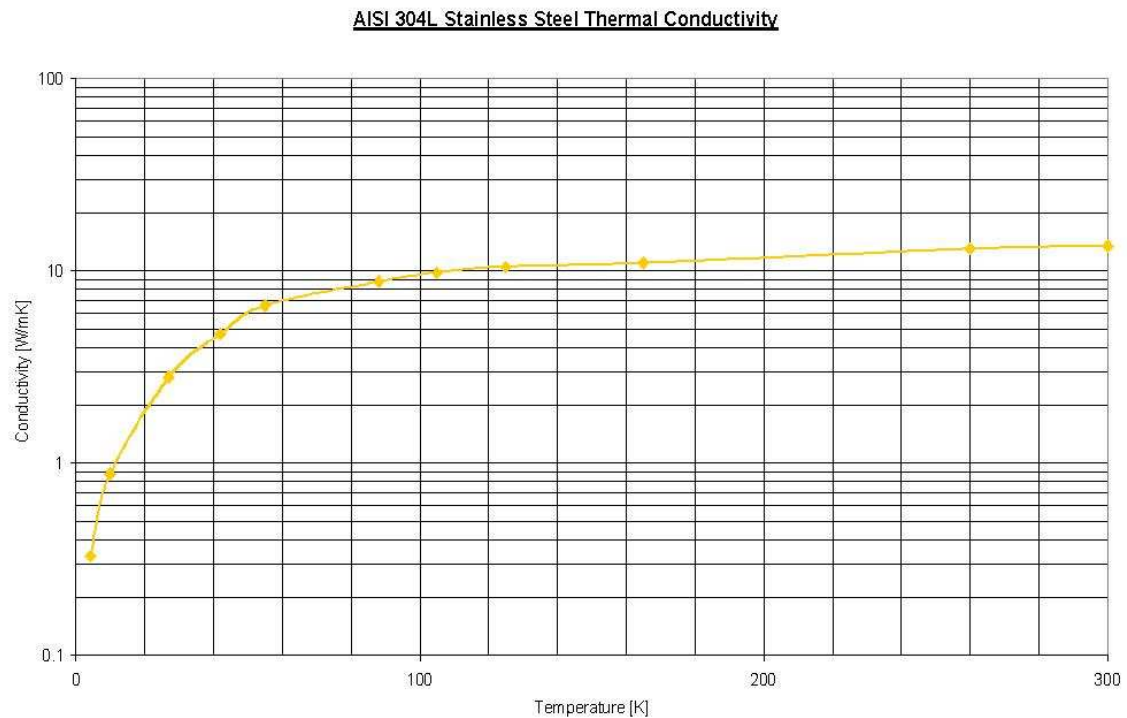


**Fig. 5:** AISI 304L Stainless Steel Thermal Conductivity.

## V. Ti 6Al-4V TITANIUM GRADE 5

Mass Density	4480	kg/m <sup>3</sup>
Elastic Strength	825	MPa
Ultimate Strength	895	MPa
Allowable Elastic Stress	275	MPa
Allowable Ultimate Stress	179	MPa
Young's Modulus	114000	MPa
Poisson's Ratio	0.31	
$\int_{80\text{K}}^{300\text{K}} k(T)d\tau$	1.35	W/m
$\int_{4\text{K}}^{80\text{K}} k(T)d\tau$	0.18	W/m

## VI. Ti 5Al-2.5Sn TITANIUM GRADE 6

Mass Density	4430	kg/m <sup>3</sup>
Elastic Strength	795	MPa
Ultimate Strength	825	MPa
Allowable Elastic Stress	265	MPa
Allowable Ultimate Stress	165	MPa
Young's Modulus	110000	MPa
Poisson's Ratio	0.31	

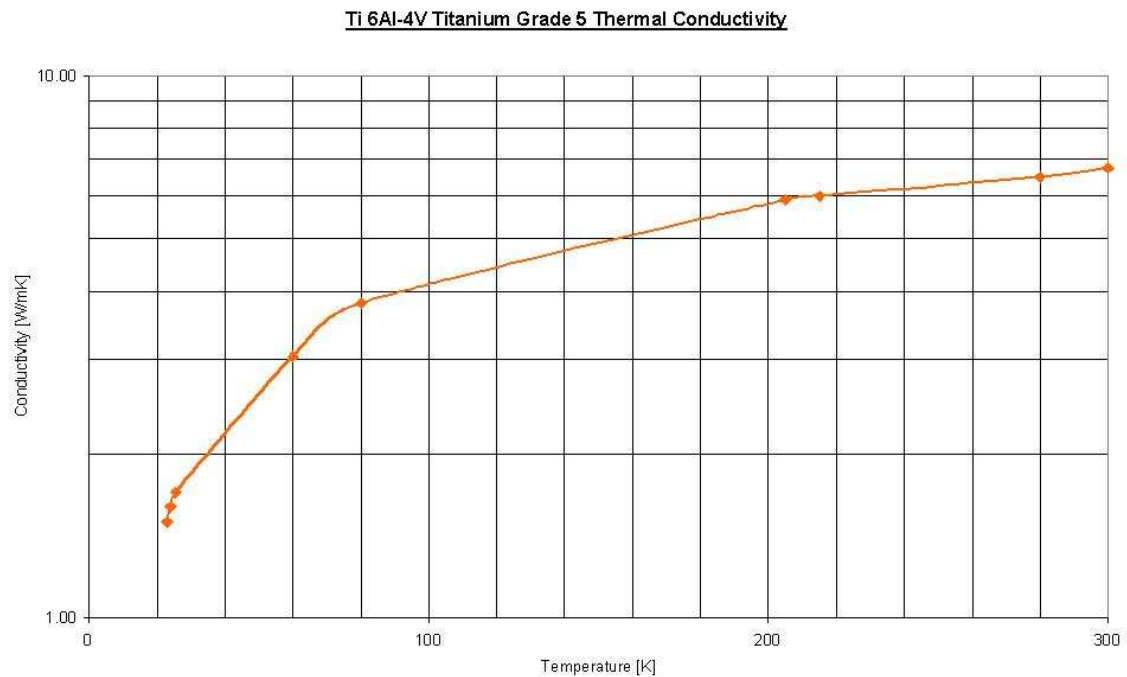


**Fig. 6:** Ti 6Al-4V Titanium Grade 5 Thermal Conductivity.

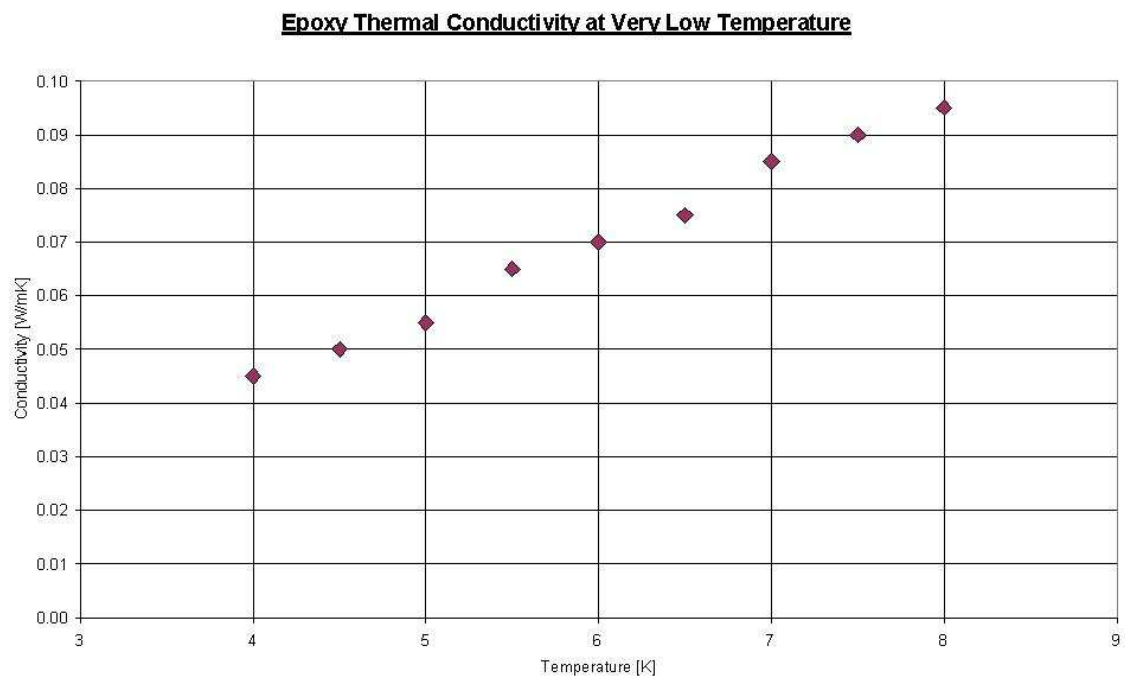


Fig. 7: Titanium Thermal Contraction.

## VII. EPOXY RESIN GLASS-FILLED

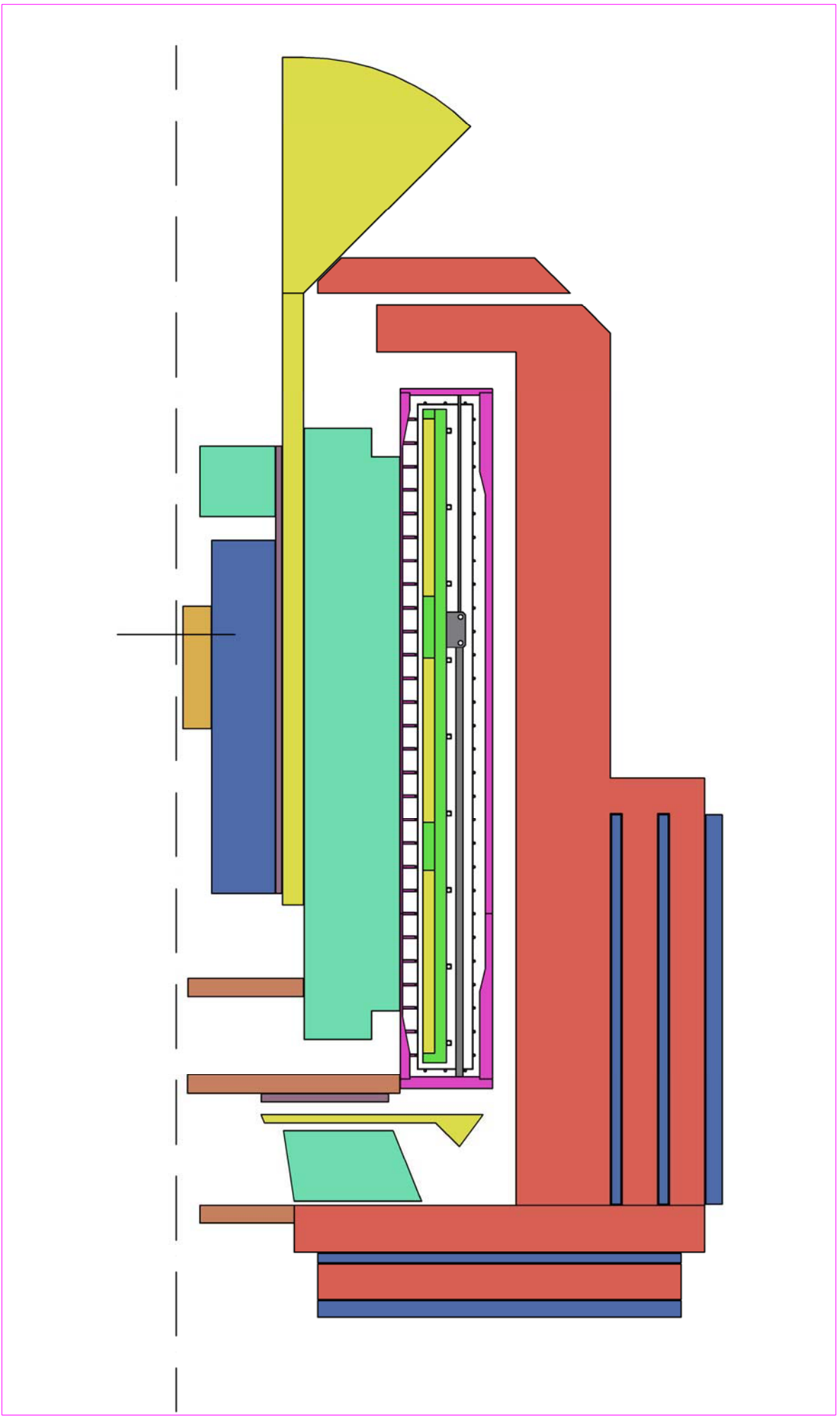
The following data are typical properties, based on a wide range of sources for Glass-Filled Epoxy Impregnation.

Mass Density	2050	kg/m <sup>3</sup>
Compressive Strength	100	MPa
Shear Strength	30	MPa
Young's Modulus	14000	MPa
Poisson's Ratio	0.2	



**Fig. 8:** Epoxy Thermal Conductivity at Cryogenic Temperature.

# Annex B: Preliminary Technical Drawings

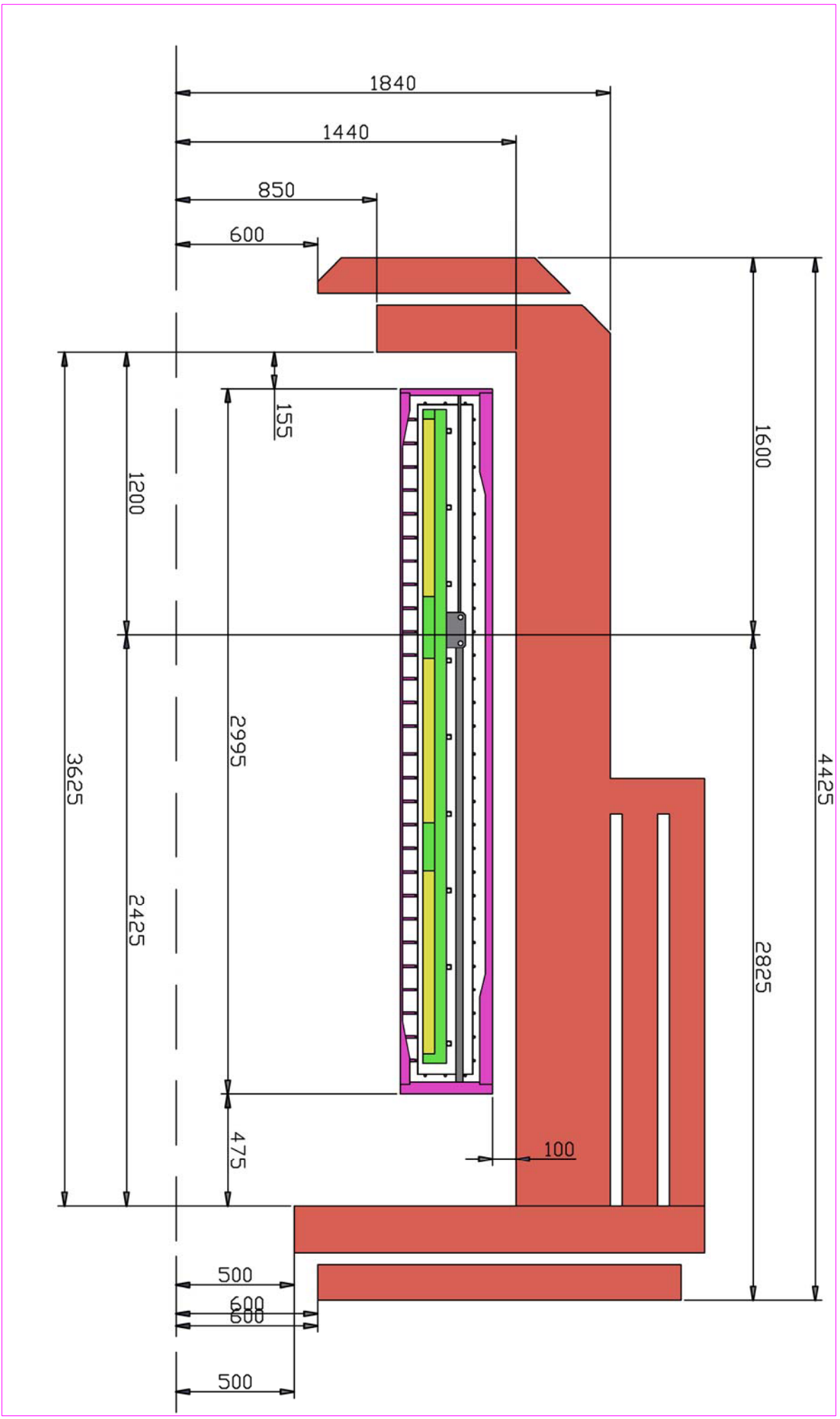


Itemref	Quantity	Title/Name, designation, material, dimension etc	Article No./Reference
Designed by A. Bersani	Checked by A. Pastorino	Approved by - date R. Parodi - 03/05/07	Date 03/05/07
File name PANDA_review			Scale n.d.

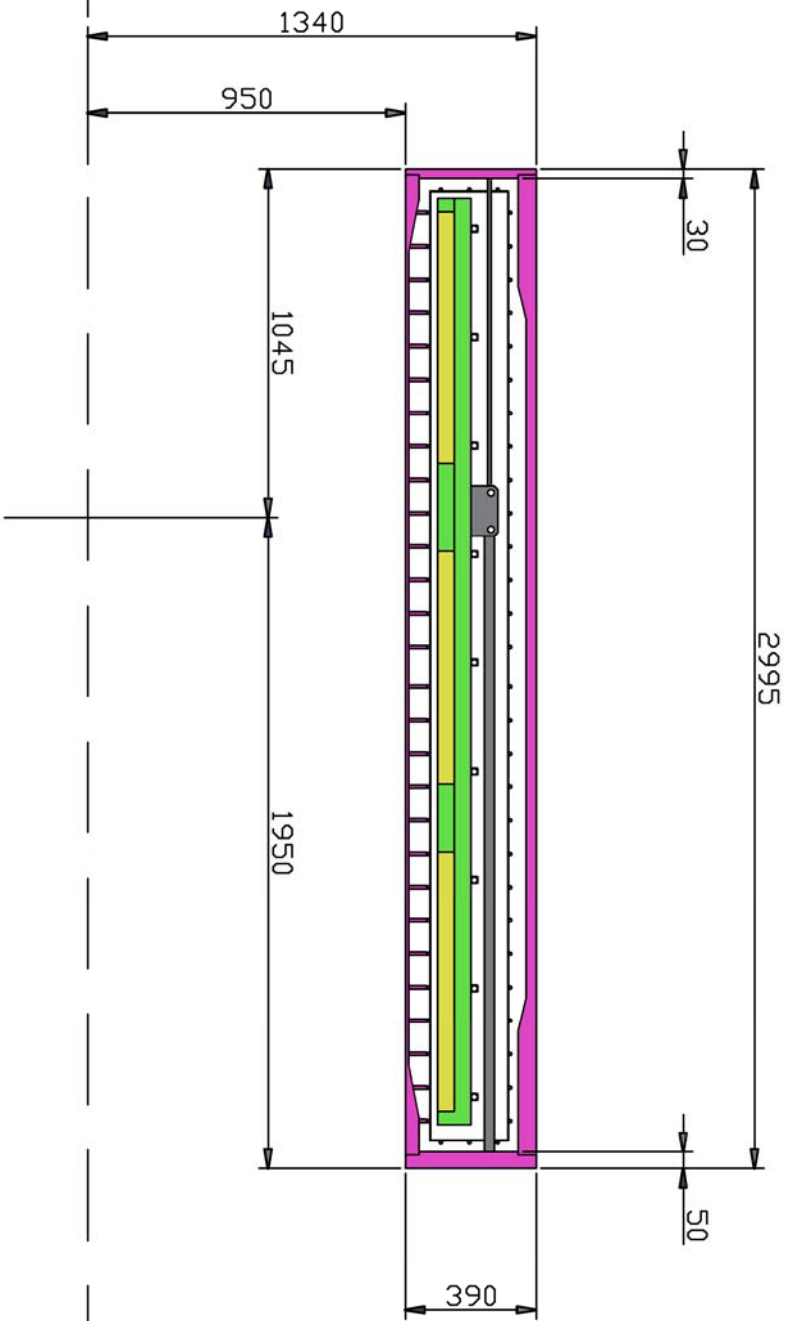
**INFN Genova**

**Ensemble**

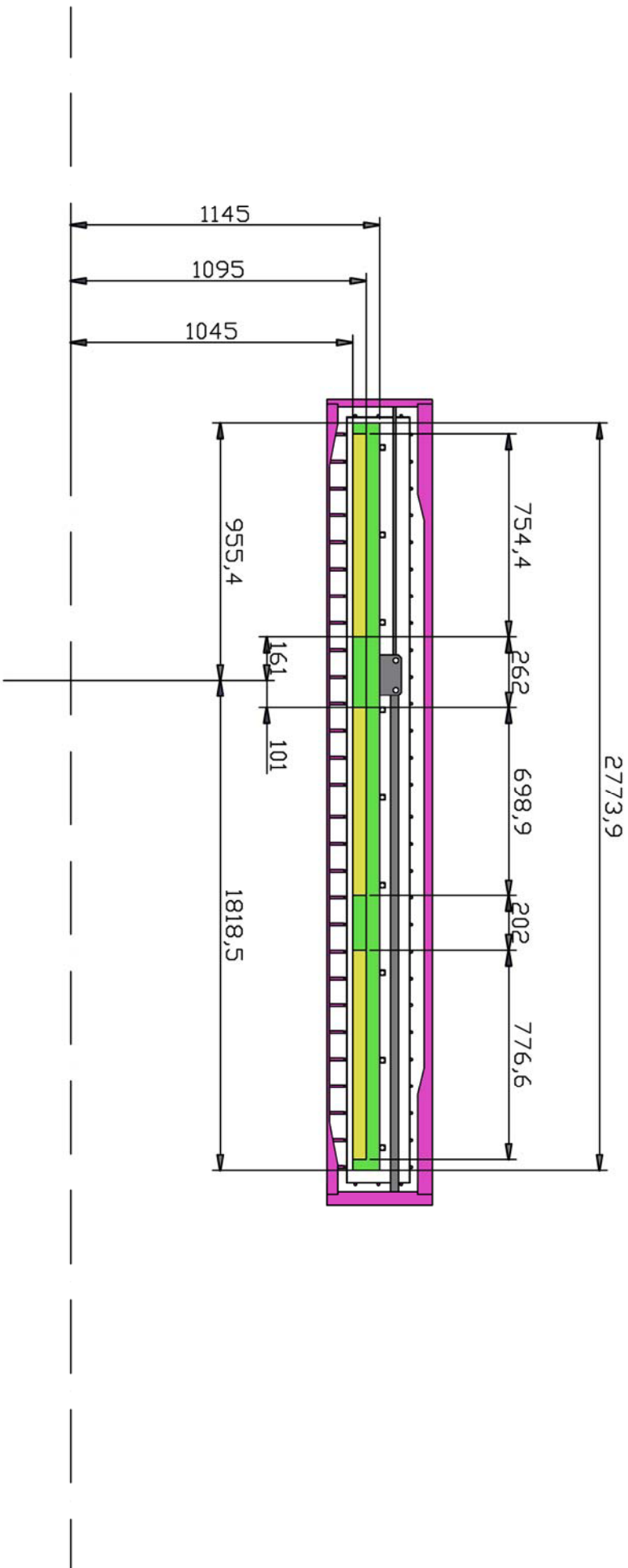
1	Edition 1.0	Sheet 1/1
---	----------------	--------------



Itemref	Quantity	Title/Name, designation, material, dimension etc	Article No./Reference
Designed by A. Bersani	Checked by A. Pastorino	Approved by - date R. Parodi - 03/05/07	Date 03/05/07
INFN Genova		File name PANDA_review	Scale n.d.
Yoke Quotes		1	Edition 1.0
			Sheet 1/1



Itemref	Quantity	Title/Name, designation, material, dimension etc	Article No./Reference
Designed by A. Bersani	Checked by A. Pastorino	Approved by - date R. Parodi - 03/05/07	Date 03/05/07
INFN Genova		File name PANDA_review	Scale n.d.
Cryostat Quotes		Edition 1.0	Sheet 1/1



Itemref	Quantity	Title/Name, designation, material, dimension etc	Article No./Reference
Designed by A. Bersani	Checked by A. Pastorino	Approved by - date R. Parodi - 03/05/07	Date 03/05/07
INFN Genova		File name PANDA_review	Scale n.d.
		Coil Quotes	
		1	Edition 1.0
			Sheet 1/1